Geochemistry, Geophysics, Geosystems®

RESEARCH ARTICLE
10.1029/2022GC010445

Mesocrystalline Architecture in Hyaline Foraminifer Shells Indicates a Non-Classical Crystallisation Pathway

A. I. Arns[1], D. Evans[2], R. Schiebel[1], L. Fink[3], M. Mezger[4], E. Alig[3], J. Linckens[2], K. P. Jochum[1], M. U. Schmidt[3], A. Jantschke[5], and G. H. Haug[1,6]

[1]Max Planck Institute for Chemistry, Mainz, Germany, [2]Institute of Geosciences, Goethe University Frankfurt, Frankfurt, Germany, [3]Institute of Inorganic and Analytical Chemistry, Goethe University Frankfurt, Frankfurt, Germany, [4]Faculty of Physics, University of Vienna, Vienna, Austria, [5]Institute of Geosciences, Johannes Gutenberg University Mainz, Mainz, Germany, [6]Department of Earth Sciences, ETH Zürich, Zurich, Switzerland

Abstract Calcareous foraminifer shells (tests) represent one of the most important archives for paleoenvironmental and paleoclimatic reconstruction. To develop a mechanistic understanding of the relationship between environmental parameters and proxy signals, knowledge of the fundamental processes operating during foraminiferal biomineralization is essential. Here, we apply microscopic and diffraction-based methods to address the crystallographic and hierarchical structure of the test wall of different hyaline foraminifer species. Our results show that the tests are constructed from micrometer-scale oriented mesocrystals built of nanometer-scale entities. Based on these observations, we propose a mechanistic extension to the biomineralization model for hyaline foraminifers, centered on the formation and assembly of units of metastable carbonate phases to the final mesocrystal via a non-classical particle attachment process, possibly facilitated by organic matter. This implies the presence of metastable precursors such as vaterite or amorphous calcium carbonate, along with phase transitions to calcite, which is relevant for the mechanistic understanding of proxy incorporation in the hyaline foraminifers.

Plain Language Summary Foraminifers are single celled marine organisms typically half a millimeter in size, which form shells made of calcium carbonate. During their life, the chemical composition of their shells records environmental conditions. By analyzing fossil shells, past conditions can be reconstructed to understand ancient oceans and climate change. To do that correctly, we need to know exactly how foraminifers form their shell. We find that foraminifers build micrometer-sized mesocrystals which are made of smaller building blocks. This means that the smallest building blocks form first and assemble to form a larger grain, which is oriented in a specific direction. To align all the building blocks, it is possible that they are first unstable and undergo transformation on assembly, during which their composition may change. By understanding and quantifying this process, the composition of the final fossil shell may be understood, ultimately leading to more reliable reconstructions of past environmental change.

Key Points:

- Hyaline foraminiferal shells are built of micrometer sized mesocrystalline units
- Biomineralization likely includes the formation and assembly of nanoparticles
- Nanometer sized units suggest non-classical crystal growth

Supporting Information:

Supporting Information may be found in the online version of this article.

Correspondence to:

A. I. Arns,
anthea.arns@mpic.de

Citation:

Arns, A. I., Evans, D., Schiebel, R., Fink, L., Mezger, M., Alig, E., et al. (2022). Mesocrystalline architecture in hyaline foraminifer shells indicates a non-classical crystallisation pathway. *Geochemistry, Geophysics, Geosystems*, *23*, e2022GC010445. https://doi.org/10.1029/2022GC010445

Received 23 MAR 2022
Accepted 16 MAY 2022

Author Contributions:

Conceptualization: A. I. Arns, D. Evans, R. Schiebel, M. U. Schmidt
Data curation: A. I. Arns, L. Fink
Formal analysis: A. I. Arns, J. Linckens, K. P. Jochum
Funding acquisition: G. H. Haug
Investigation: A. I. Arns, L. Fink, M. Mezger, E. Alig, J. Linckens
Methodology: A. I. Arns, L. Fink, E. Alig, J. Linckens, M. U. Schmidt
Project Administration: R. Schiebel
Resources: D. Evans, R. Schiebel, M. Mezger, J. Linckens, K. P. Jochum, M. U. Schmidt, G. H. Haug
Software: M. Mezger
Supervision: D. Evans, R. Schiebel, M. U. Schmidt

1. Introduction

Calcareous foraminifers are an abundant group of planktic and benthic marine unicellular organisms, which together constitute an important component of the global carbon cycle (Langer, 2008; Schiebel, 2002). Foraminifer shells (tests) can resist dissolution and diagenesis over millions of years, and hence provide an outstanding archive for climate reconstruction at high time resolution from sediment cores, which is possible via empirical calibration of chemical or physical characteristics of the shells of recent species (e.g., Fischer & Wefer, 1999; Katz et al., 2010). Despite their importance as a paleoclimate archive, the biomineralization of foraminifers is not mechanistically understood in detail, which leaves the fundamental relationship between environmental parameters and proxy data enigmatic. For example, the possible presence of residues of metastable carbonate phases such as vaterite was only recently discovered (Jacob et al., 2017), and the delivery of ions to the biomineralization site is an ongoing topic of debate (Bentov & Erez, 2006; Bentov et al., 2009; de Nooijer et al., 2014; Evans et al., 2018; Nehrke et al., 2013; Toyofuku et al., 2017).

The focus of this study are the hyaline calcareous foraminifers, which includes all planktic and the majority of benthic species (Loeblich & Tappan, 1984). In contrast to the miliolid foraminifers (discussed elsewhere, see e.g., Bé et al., 1979; Berthold, 1976; Debenay et al., 2000; Hemleben et al., 1986; Towe & Cifelli, 1967), the

Validation: A. I. Arns, D. Evans, R. Schiebel, L. Fink
Visualization: A. I. Arns
Writing – original draft: A. I. Arns
Writing – review & editing: A. I. Arns, D. Evans, R. Schiebel, L. Fink, M. Mezger, J. Linckens, K. P. Jochum, M. U. Schmidt, A. Jantschke

source of ions in hyaline foraminifer biomineralization is likely derived mainly from vacuolised seawater, which is transported through the cell cytoplasm towards the newly forming chamber (Bentov et al., 2009; de Nooijer et al., 2009, 2014; Erez, 2003; Evans et al., 2018; Khalifa et al., 2016). In addition, trans-membrane transport (TMT) of ions via ion pumps or channels has been suggested to be the major source of ions in some species (Nehrke et al., 2013). Seawater transport to the biomineralization site is known to occur, as large membrane-impermeable fluorescent molecules from labeled seawater are incorporated into test calcite (Bentov et al., 2009; Evans et al., 2018; Khalifa et al., 2016). The seawater chemistry inside the vacuoles or at the calcification site is known to be adjusted by the organism, which has been shown directly in the case of pH elevation (Bentov et al., 2009; de Nooijer et al., 2009; Toyofuku et al., 2017), and inferred in the case of some ion concentrations, such as for Mg^{2+} (Bentov & Erez, 2006; de Nooijer et al., 2014; Erez, 2003; Evans et al., 2018). Compositional differences between the hyaline tests of low-Mg calcite planktic species and high-Mg calcite benthic species suggest differences in biochemical mechanisms or a different extent of utilization of intracellular ion dispensation pathways in these groups (Evans et al., 2018; van Dijk et al., 2017).

Based on light-microscopy observations and electron backscatter diffraction (EBSD) measurements, which show an alignment of test crystallite *c*-axes towards the outer surface of the chamber in hyaline planktic and benthic foraminifers, it has been hypothesized that organic layers act as a template for the directed crystallisation of foraminifer test calcite (Read, 2019; Towe & Cifelli, 1967; Weiner & Lowenstam, 1986; Yin et al., 2021). To date, investigations in (mostly) benthic foraminifer species reveal that the organic matter occluded in the test calcite contains sulfonated polysaccharides and a variety of proteins and polypeptides, but neither the exact role nor location of these macromolecules in the biomineralization process have yet been identified (Frontalini et al., 2019; King & Hare, 1972; Nagai, Uematsu, Chen, et al., 2018; Nagai, Uematsu, Wani, et al., 2018; Ní Fhlaithearta et al., 2013; Robbins & Brew, 1990; Robbins & Donachy, 1991; Sabbatini et al., 2014; Stathoplos & Tuross, 1991; Tyszka et al., 2021; Weiner & Erez, 1984).

The observation of metastable vaterite in the tests of planktic foraminifers suggests that the formation of the final Mg-calcite can progress via the transformation of metastable carbonate phases (Jacob et al., 2017). These may emerge as a remnant intermediate stage from the formation of amorphous $CaCO_3$ (ACC) and subsequent transformation into calcite. Formation and transformation of amorphous precursors as part of the biomineralization mechanism have been observed in a variety of organisms, and can be indicated by the presence of nanogranular fracture surfaces in the final shell ultrastructure (Addadi et al., 2003; MacIás-Sánchez et al., 2017; Raz et al., 2003; Rodríguez-Navarro et al., 2016; Seto et al., 2012; Wolf et al., 2016; 2021). A connection between non-classical crystal growth mechanisms of carbonates via attachment of nanoparticles, such as stabilized ACC, and a nanogranular morphology of the resulting crystal surface has been shown in numerous examples in precipitation experiments (e.g., De Yoreo et al., 2015; Gal et al., 2014; Rodriguez-Navarro et al., 2016; Seto et al., 2012; Sturm & Cölfen, 2016; Wolf et al., 2016). If the nanoparticular building units are crystallographically aligned within a larger framework, the resulting structure is a mesocrystal, which can result from oriented attachment of crystalline units or *in-situ* crystallisation of metastable precursor phases (Cölfen & Antonietti, 2005; Jehannin et al., 2019; Kim et al., 2014; Rao & Cölfen, 2017; Seto et al., 2012; Sturm & Cölfen, 2016).

The aim of this study is to assess biomineralization mechanisms of hyaline foraminifers based on the relation of nano-to mesosized structures, and to interpret the resulting structure-to-composition connections. To this end, the hierarchy and structural organization of the hyaline foraminiferal test calcite ultrastructure was analyzed crystallographically and microscopically at the nano- and mesoscale, including an estimation of the crystallite domain size, and contrasted to nanoscale aspects of miliolid tests. We discuss the implications of these findings for the possible involvement of amorphous and metastable crystalline precursor phases in the biomineralization process, as well as for the possible mechanisms of test formation.

2. Materials and Methods

2.1. Samples

The low-Mg calcite planktic foraminifers *Globigerinoides ruber ruber* and *Globigerinoides ruber albus* (sensu stricto, s.s.; Morard et al., 2019), *Trilobatus sacculifer*, *Globigerina bulloides* and the low-Mg calcite benthic *Cibicidoides wuellerstorfi* were selected from seafloor surface sediments obtained during R/V M.S. Merian Cruise MSM58 in the Madeira Basin (MSM58-57-1) at 0–15 cm sediment depth (Repschläger et al., 2018). Specimens

were picked from the 315–400 μm size fraction and washed with distilled water. From the same sample, specimens of the high-Mg calcite (miliolid or 'porcelaneous') *Pyrgo* sp. were picked to provide a comparison to the hyaline foraminifer tests. Live specimens of the hyaline low-Mg calcite planktic *G. ruber albus* were collected in 2019 from the North Atlantic (29.507°N, 15.005°W) from a water depth of 30–40 m with the research vessel S/Y Eugen Seibold. The samples were stored in hexamine buffered formalin solution at pH 8.2 at 4°C, picked, dried, and stored in microslides prior to analysis. Live specimens of the high-Mg calcite benthic foraminifer *Operculina ammonoides* were collected from a water depth of 20 m at Kepulauan Seribu, Jakarta (see sample SER in Evans et al., 2013). Tests of the high-Mg calcite benthic foraminifer species *Amphistegina lessonii* were collected from the Gulf of Aqaba/Eilat. The living benthic specimens were rinsed with tap water and the tests were stored dry at room temperature and ambient humidity prior to analysis. For comparison, fossil *G. ruber* specimens were picked from the Caribbean ODP Site 999A (10 H 04 35-37) from size fraction 315–400 μm. The age of the fossil 999A sample is 5.6 Ma (Öğretmen et al., 2020).

2.2. Electron Microscopy Assessment of Foraminifer Chamber Walls

Foraminifer tests were imaged by scanning electron microscopy (SEM) at the Max Planck Institute for Chemistry, using a Zeiss Leo 1530 field emission scanning electron microscope. The samples were sputtered with 15 nm gold. Maximum magnification was 85000×, and the minimum pixel size was 4 nm. Chambers were mechanically cracked using a preparation needle and placed on a carbon tape-coated sample holder stub with the fracture surface facing upwards to facilitate inspection of the internal structure of the chamber wall.

2.3. Electron Backscatter Diffraction on Foraminifer Test Walls

Electron Backscatter Diffraction (EBSD) measurements were conducted using a JEOL JSM 6490 SEM equipped with an HKL Nordlys EBSD detector at the Institute of Geosciences at Goethe University Frankfurt. A live-collected specimen of *G. ruber albus* was embedded in low-viscosity vacuum stable epoxy resin, gradually polished down (3 μm diamond paste, 1 μm diamond paste, 0.25 μm diamond paste, and 15 min of colloidal silica) and coated with carbon prior to measurement. Measurements were performed nearly perpendicularly to the chamber wall, enabled by careful polishing. The electron beam was set at an acceleration voltage of 15 kV, a beam current of ∼8 nA, and a working distance of 17–20 mm. Detailed investigations of selected sections were carried out at 0.2 μm step size. Data processing and indexing was conducted with the Channel5 software (Schmidt & Olesen, 1989), and included removal of wild spikes, filling of non-indexed pixels using five nearest neighbor approximation algorithms and autodetection of grains under the assumption of a grain boundary misorientation of >10°. One point per grain was selected to plot on an upper hemisphere equal area pole figure and contoured using a halfwidth of 15°. A calcite structure model was used for indexing, with Euler angle coloring used to display the crystallographic orientation.

2.4. Femtosecond Laser Ablation Inductively Coupled Plasma Mass Spectrometry (fs-LA-ICP-MS)

Laser Ablation Inductively Coupled Plasma Mass spectrometry (LA-ICP-MS) measurements on single foraminifer chambers were conducted at the Max Planck Institute for Chemistry. Analysis of ^{23}Na, ^{25} Mg, ^{43}Ca, and ^{88}Sr were performed using a sector-field Thermo Element2 ICP-MS coupled to a 200 nm femtosecond laser ablation system (NWRFemto200), which has a pulse width of 130 fs. The laser spot size was set at 45 μm diameter. Ablation was conducted using a repetition rate of 15 Hz and 45 s ablation time, using He (0.7 l min^{-1}) as a carrier gas. The ThO/Th rate was <1%, at an RF power of 1078 W and Ar sample flow rate of 0.6 l min^{-1}. The synthetic silicate glass NIST SRM612 (Jochum et al., 2011) and pressed carbonate powder MACS-3 (Jochum et al., 2019) were used as reference materials and measured repeatedly in the same way as the samples. The foraminifers were placed in a sandbox containing pure quartz grains >250 μm during laser ablation. The penultimate (F-1) chamber of three specimens per species was targeted for analysis. The signal was limited to the bulk chamber wall to exclude portions that can be attributed to either encrustation on the outer surface or possible contamination by sedimentary particles on the inside of the chamber. Data evaluation included gas blank subtraction, normalization to an internal standard (^{43}Ca), and external calibration to NIST SRM612, using the NIST values of Jochum

et al. (2011) and the NIST Mg values of Evans and Müller (2018), following standard data reduction procedures (Heinrich et al., 2003). Accuracy, determined as measured/reported molar M/Ca values for MACS-3 from Jochum et al. (2019), was 0.939 for Na/Ca, 1.079 for Mg/Ca, and 0.886 for Sr/Ca. Precision, defined as 2 SD/mean of repeatedly measured molar M/Ca, ranged between 11.2% and 13.2% for the discussed ratios of MACS-3.

2.5. X-Ray Diffraction Measurements (XRD)

2.5.1. Bulk Foraminifer XRD

X-ray powder diffraction (XRD) measurements of bulk foraminifer samples were conducted on whole-shell monospecies assemblages, which contained up to 400 tests, depending on size of the specimens. The foraminifer samples were measured in rotating glass capillaries (ø = 0.7 mm) for bulk multi-specimen analyses. In the case of measurements conducted on samples that consisted of a small number of rather large individuals (3–10 tests of *O. ammonoides* and *A. lessonii*), the tests were crushed and filled in a small capillary (ø = 0.5 mm), which was placed and adjusted inside the 0.7 mm capillary. The measurements were performed in Debye-Scherrer geometry on a STOE STADI-P transmission diffractometer, using Mo-$K_{\alpha 1}$ ($\lambda = 0.70930$ Å) and Cu-$K_{\alpha 1}$ ($\lambda = 1.5406$ Å) radiation at the Institute of Inorganic and Analytical Chemistry, Goethe University Frankfurt. The instruments were equipped with a curved Ge (111)-monochromator and a Mythen 1K or linear PSD detector. For Mo-radiation, the measured range was 0–100° 2θ in 0.015° steps, at a Mythen 1K step size of 0.49° and an exposure time of 60.0 s per step. For Cu-radiation, the measured range was 2–115° 2θ in 0.010° steps, at a PSD step size of 0.2° and an exposure time of 25.0 s per step. The 2θ range was measured repeatedly (2 × 0–100° 2θ, 2 × 40–100° 2θ and 2 × 80–100° 2θ for Mo and 2 × 2–115° 2θ, 2 × 40–115° 2θ and 2 × 80–115° 2θ for Cu), following which the single ranges were combined to a high-quality data set suited for pair distribution function (PDF) calculations. Using the same measurement parameters and instrument geometry, the respective empty capillaries were measured for background determination. The data were processed with the Stoe $WinX^{POW}$ software (STOE & Cie GmbH, 2011). For comparison, pieces of a large (~5 cm) translucent birefringent rhombohedral geological calcite crystal were carefully ground and measured in the same way as the foraminifer samples.

2.5.2. Single Specimen Diffraction Measurements

Qualitative analyses of 1–3 specimens of live and fossil *G. ruber* were conducted using a Rigaku SmartLab diffractometer at the Max Planck Institute for Polymer Chemistry, Mainz, equipped with a Mo-$K_{\alpha 1}$ source and a HyPix-3000 2-dimensional semiconductor detector. The measurement time was 120 min and the measured range for this geometry was 5.5–60° 2θ. Foraminifer specimens were placed in stationary 0.3 mm glass capillaries and measured in transmission. An empty capillary and a LaB_6 standard were measured using the same setup for background correction and calibration, respectively. The resulting 2D detector images of the foraminifer samples were calibrated for the instrument geometry using the known reflex positions of the LaB_6 standard material, radially integrated, and corrected for background scattering of air and sample holder using an internal Python script.

2.6. Processing of Diffraction Data

Rietveld refinement of the measurements with Cu-radiation were conducted using TOPAS 6 academic (Coelho, 2016b). The size of the coherently scattering domain was refined by starting from a structural model of calcite (Graf, 1961) followed by stepwise release of parameters for scale, zero error, background, instrumental corrections using a full axial model, unit cell dimensions, and crystallite size and strain to yield a reproducible fit with a goodness-of-fit value close to 1 (Table S2 in Supporting Information S1). The domain size was determined from the integral breadth of the strongest reflexes (20–52° 2θ), using a Gaussian peak shape. The error of the crystallite size given below is the convolution of errors of the measurement and the refinement procedure, which is lined out in detail in the TOPAS 6 technical reference (Coelho, 2016a).

The pair distribution function G(r) was calculated for a radius of 1000 Å using the program pdfgetX3 (Juhás et al., 2013) from corrected and normalized 1D Mo XRD data (Egami & Billinge, 2003). Background corrections for detector noise, air scattering and contributions of the empty capillary were either performed beforehand by 1:1 signal to background reduction, or by using pdfgetX3 for adjustments. The total

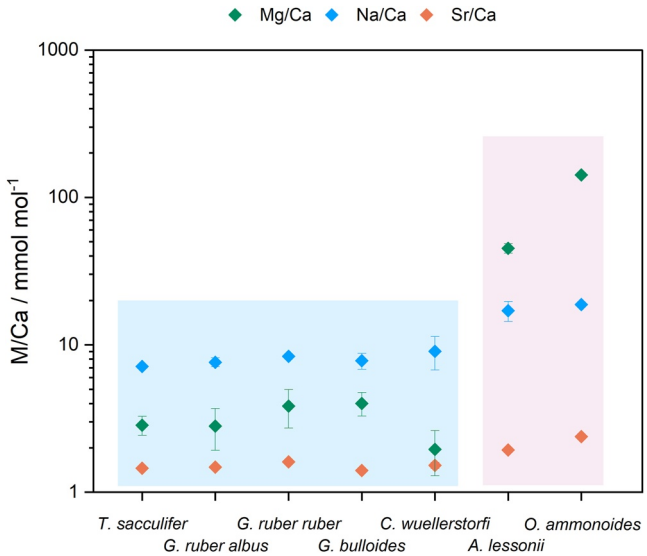

Figure 1. Composition of bulk test walls for the investigated foraminifer species, averaged over all specimens of one species. The error bars indicate the range of measured values of different specimens of one species. Low-Mg calcite species are highlighted in blue and high-Mg calcite benthic species in red.

scattering structure function F(Q) was adjusted with the program-internal polynomial fitting factor r_{poly} to yield a signal oscillating around 0 (Juhás et al., 2013). The data range was truncated both at small and large wavevector Q, to exclude measurement artifacts and to adjust the shortest distances in the PDF to chemically meaningful values. The maximum momentum transfer Q_{max} was chosen at the maximum value that yields stable signals in the calculated G(r), which was Q_{max} = 13.0–13.5 Å for Mo-$K_{\alpha 1}$. The electron density of the foraminifer tests was estimated from averaged LA-ICP-MS analyses of the chamber composition. The ordering length resolvable with this method, that is, the minimal domain size of coherently scattering atoms within a crystallite, was approximated from the smallest interatomic distance at which oscillation of constant frequency allocated to artifacts from the Fourier transformation was observed. As such, long-range PDF supports crystallite domain size determination by Rietveld refinement.

3. Results

3.1. Elemental Composition of Foraminifer Tests

The test metal/Ca (M/Ca) composition of the investigated hyaline planktic and benthic foraminifers differs between low-Mg calcite and high-Mg calcite (Figure 1), as observed previously (e.g., Allen et al., 2016; Evans et al., 2018; Geerken et al., 2019; van Dijk et al., 2019). Planktic foraminifers (all low-Mg calcite, blue) and the low-Mg calcite benthic *C. wuellerstorfi* are characterized by a Mg/Ca of 2–5 mmol mol^{-1}. The high-Mg calcite producing benthic species (red) range between a Mg/Ca of 40–50 mmol mol^{-1} (*A. lessonii*) and 135–145 mmol mol^{-1} (*O. ammonoides*). Sr/Ca and Na/Ca are elevated in high-Mg calcite benthic species compared to low-Mg calcite species by a factor of approximately two (Figure 1).

3.2. Diffraction Measurements

3.2.1. Crystallographic Structure of Foraminifer Test Carbonates

Planktic and benthic foraminifer species consist of low-Mg and high-Mg calcite as primary (ontogenetic) shell material, as demonstrated by many previous studies (e.g., Berman et al., 1993; Blackmon & Todd, 1959; Debenay et al., 2000; Read, 2019; Towe & Cifelli, 1967) and confirmed here by XRD analyses (Figure 2a). Additional reflections and metastable crystalline carbonate phases, if present, were not observable above the detection limit in XRD measurements for the hyaline species. A faint amorphous background is visible in the XRD of live collected benthic foraminifers (Figure 2a) but is not resolvable in the live collected *G. ruber albus* (Figure 2b). Specimens of both *G. ruber* subspecies of different preservation stage, that is, live collected/surface sediment/fossil (sediment core, approx. age 5.6 Ma), consist of low-Mg calcite without resolvable metastable carbonate or secondary diagenetic crystalline phases (Figures 2a and 2b). Due to uncertainties regarding the exact location of the specimen in the sample holder and the small sample size and thus low intensities, confident analyses of live collected and fossil *G. ruber albus* are limited to qualitative assessment of the crystalline content and do not extend to the amorphous background.

Unit cell dimensions, as determined by Rietveld refinement, are similar for all low-Mg calcite species (Table 1, Figure 2c). In the case of the hyaline benthic species *C. wuellerstorfi*, the refined *a* dimension of the test calcite is significantly larger ($|a_{geolog.}\text{-}a_{foram.}| > 5$ SD, Table 1) than that of geological calcite (Graf, 1961). For *G. ruber albus*, the same is observed, albeit non-significantly (Table 1). The high-Mg calcite species show considerably smaller lattice parameters caused by the smaller size of the Mg^{2+} ion incorporated in the structure. Refined average crystallite domain sizes of the foraminiferal calcites range between 70 and 85 nm for all investigated species, except for *C. wuellerstorfi* with crystallite domains of approximately 145 nm (Table 1, Figures 2c and 2d).

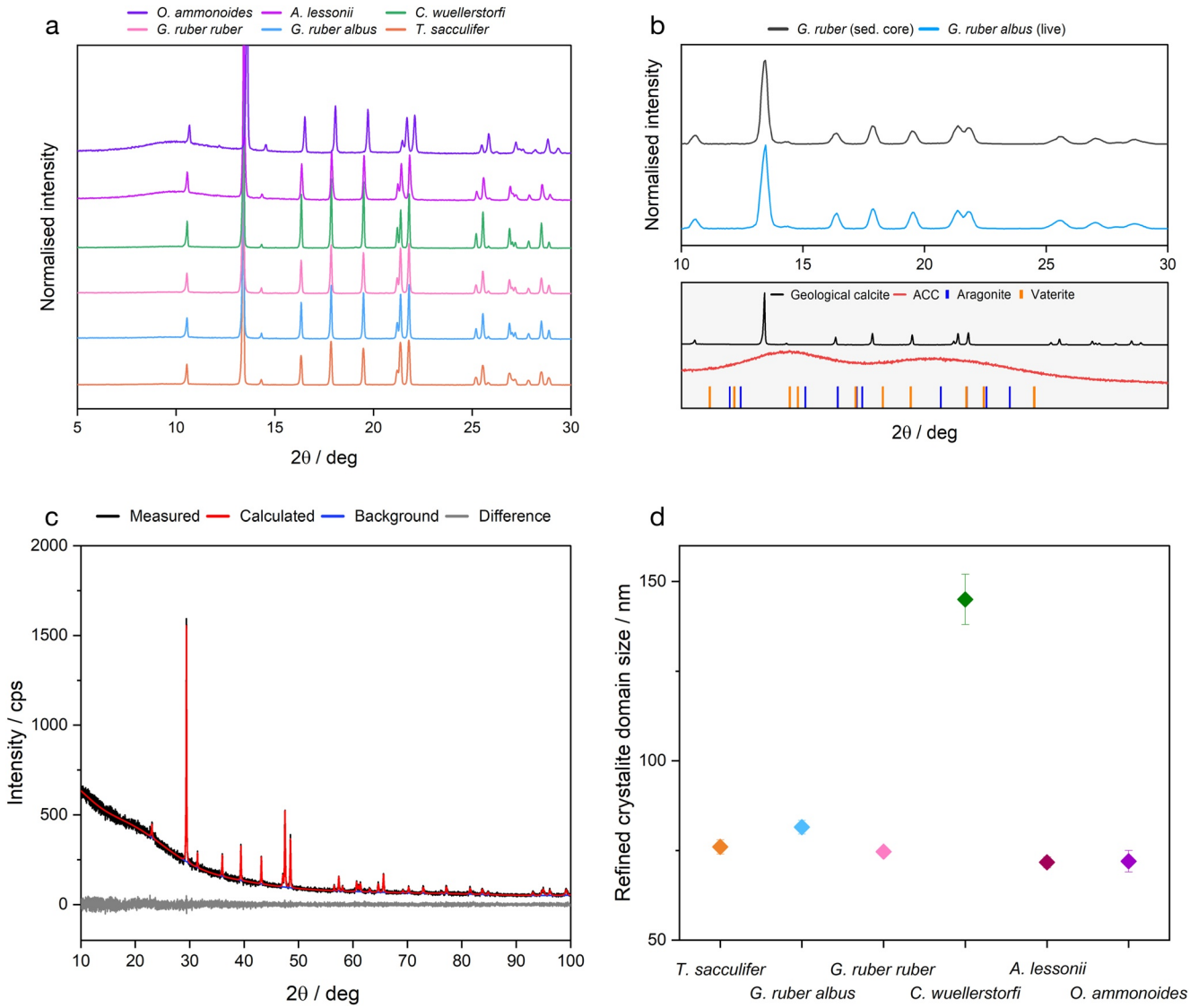

Figure 2. (a) X-ray powder diffraction (XRD) measurements (Mo-$K_{\alpha 1}$ radiation) of hyaline bulk foraminifer samples consisting of up to ~400 specimens. Intensities are normalized for comparison. (b) Detail of Mo-$K_{\alpha 1}$ radiation XRD measurement of single specimens of fresh and fossil *G. ruber albus*. Geological calcite is shown for comparison, along with a reference pattern for amorphous $CaCO_3$ (ACC) precipitated from seawater (transformed to Mo-radiation from Evans et al., 2019), as well as tick marks of the most intense reflections of aragonite (De Villiers, 1971) and vaterite (Wang & Becker, 2009). (c) Example Rietveld refinement of Cu-$K_{\alpha 1}$ radiation XRD of *G. ruber albus* with measured and calculated pattern as well as difference curve. (d) Crystallite domain size of hyaline foraminiferal calcite as determined by Rietveld refinement. Error bars represents 1 SD and are smaller than the symbol size in most cases.

3.2.2. Pair Distribution Function Analysis

The pair distribution function (PDF) describes the probability of finding two atoms with an atom-atom distance r. The PDF is weighted with the scattering power of the two atoms and summed over all atom-atom pairs. The signal position and shape of short- and mid-range atomic distances (<20 Å) in the PDF of hyaline planktic low-Mg calcite foraminifers are similar, without visible deviations of the peak geometry within one data set (Figure 3a). In *C. wuellerstorfi* and *T. sacculifer*, individual signals differ from each other in shape, and signal broadening is observed, for example, for signals at 4.1, 9.5, and 12.9 Å (Figure 3a). In the high-Mg calcite species, peak shape and center of gravity differ to signals observed in low-Mg foraminiferal calcite, for example, for interactions at 3.1–3.5 (Ca-C), and 4–4.5 Å (incl. Ca-Ca, Figure 3a). An additional signal is present at 1.6 Å in both *A. lessonii* and *O. ammonoides*, which is not present in the other samples (Figure 3a).

Table 1
Lattice Parameters and Crystallite Domain Sizes as Derived From Rietveld Refinement for Foraminiferal Test Calcite

Species	Mg/Ca/ mmol mol^{-1}	*a*/Å	*c*/Å	Crystallite domain size/nm
T. sacculifer	3.11	4.9874(5)	17.0567(14)	76(2)
G. ruber albus	2.81	4.9912(5)	17.0679(13)	81.5(19)
G. ruber ruber	3.85	4.9854(5)	17.0505(16)	74.7(12)
C. wuellerstorfi	1.95	4.9919(3)	17.0647(10)	145(7)
A. lessonii	45.0	4.9842(7)	17.033(2)	71.7(15)
O. ammonoides	141.8	4.9289(17)	16.776(5)	72(3)
Geological calcite		4.9900	17.0615	

Note. The Mg/Ca data represent a species-specific average calculated from the LA-ICP-MS data (Table S1 in Supporting Information S1). Errors in parentheses are given as 1 SD of the refinement with respect to the last digit. Geological calcite structure from Graf (1961).

The long-range PDF signals decay strongly in intensity for all hyaline foraminifers between 50 and 400 Å, with the presence of structure-related signal terminating at approximately 300–500 Å (30–50 nm, Figure 3b).

3.3. Scanning Electron Microscopic Imaging of Fractured Foraminifer Tests

Optical assessment of the foraminifer test walls shows distinct shell architectures for porcelaneous and hyaline foraminifers, as well as differences between high-Mg calcite benthic species and low-Mg calcite planktic foraminifers (Figure 4). The bulk test walls of the hyaline low-Mg planktic species are characterized by irregularly shaped entities ranging between 50 and 150 nm in size, which are predominantly spherical, and partly elliptical (Figure 4). No crystal facets, that is, edges or distinct surfaces are visible on these building blocks in the freshly fractured test wall. Residues of spines, which are embedded in the wall of spinose species, exhibit a smooth surface and distinct crystal facets at the tips (Figure S1 in Supporting Information S1). In *T. sacculifer*, the outer 0.5 µm of the test wall at a region close to the aperture shows planar surfaces and edges resembling crystal features, and no identifiable nanogranular internal morphology (Figure S1 in Supporting Information S1). In the investigated hyaline benthic species, two types of irregularly shaped entities are observed, which either range in size between 50 and 150 nm or several hundreds of nanometers in diameter (Figure 4). They appear to be either rounded or show faces and edges (Figure 4). The test wall of the miliolid *Pyrgo* sp. is made of elongated crystals of approximately 300–2000 nm length and 100 nm diameter. Distinct crystal facets are visible both at the rims and ends of the crystals (Figure 4).

3.4. Electron Backscatter Diffraction (EBSD) of Polished Foraminifer Chamber Walls

An EBSD map of the test wall of the hyaline *G. ruber albus* shows differently sized grains of mostly elongated and partly irregular shape, ~3–10 µm in diameter (gray areas in the band contrast image, Figure 5a). A defined

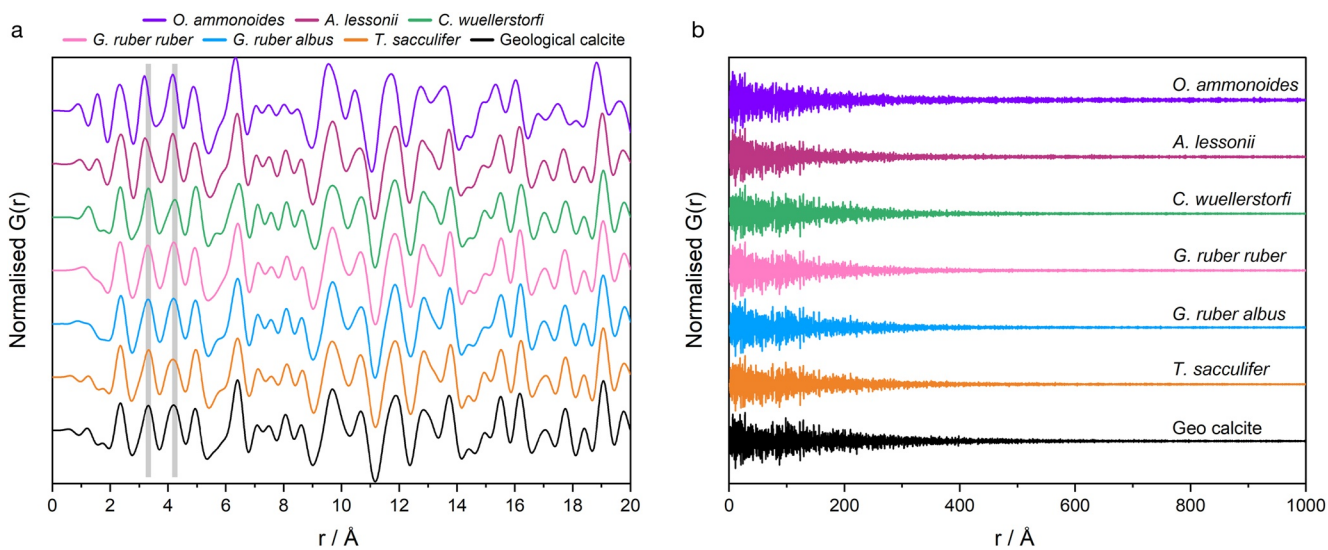

Figure 3. Pair distribution function (PDF) calculations from bulk X-ray powder diffraction measurements for (a) short- and mid-range and (b) long-range interatomic distances of different foraminifer species, indicated in different colors. A geological calcite is displayed for comparison. In panel a, signals at 3.0–3.5 Å (Ca-C) and 3.9–4.4 Å (Ca-Ca) are highlighted by gray bars. PDFs are normalized to 1 for comparison.

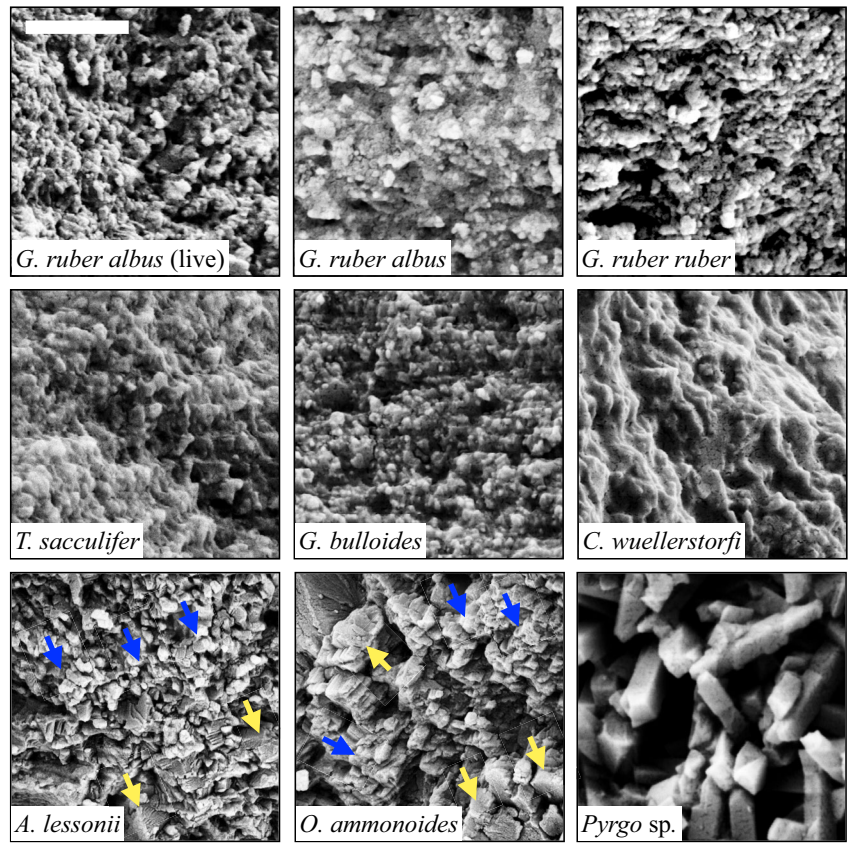

Figure 4. Scanning electron microscopy images of the freshly fractured test walls of different benthic and planktic foraminifer species. Nanogranular morphologies are clearly visible as the predominant building unit in all hyaline planktic species and as part of the internal architecture in hyaline benthic species (blue arrows), in contrast to the miliolid species (*Pyrgo* sp.). Yellow arrows highlight larger structures present in hyaline benthic foraminifers. Scale bar (upper left corner) applies to all micrographs and is 1 μm.

orientation towards the outer surface of the chamber wall is present for the crystallographic *c*-axis {0001} of the calcite grains, as indicated by uncolored regions of similar coloration and in the upper hemisphere plot, whereas the *a*-axis {11–20} is randomly oriented (Figures 5b and 5c). The orientation of the analyzed specimen with respect to the polished surface is slightly tilted such that the map is not exactly perpendicular to the shell surface. Large parts of the test wall were not recognized as calcite by the automated indexing protocol (Figure 5).

4. Discussion

4.1. Metastable and Amorphous Carbonates in Foraminifer Tests

The presence of crystalline metastable carbonate phases is not observed with the setup utilized here for hyaline species, even in specimens that were collected live (Figures 2a and 2b), that is, *G. ruber albus*, *A. lessonii*, and *O. ammonoides*. The specimens were stored under normal atmospheric conditions in plastic containers in the case of the high-Mg benthic foraminifers, and in formalin solution at 4°C in the case of *G. ruber albus*. As such, unintended initiation of a phase transition of metastable carbonates to calcite after collection is considered unlikely for the high-Mg benthic species, but possible in the case of *G. ruber albus*. Phase transformations in the $CaCO_3$ system can be initiated by, e.g., heating, application of mechanical energy, or placement in solution (e.g., Bots et al., 2012; Konrad et al., 2018; Ogino et al., 1987; Rodriguez-Blanco et al., 2011; Spanos & Koutsoukos, 1998). With the XRD setups used in this study the detection limit for crystalline phases is normally <1% such that

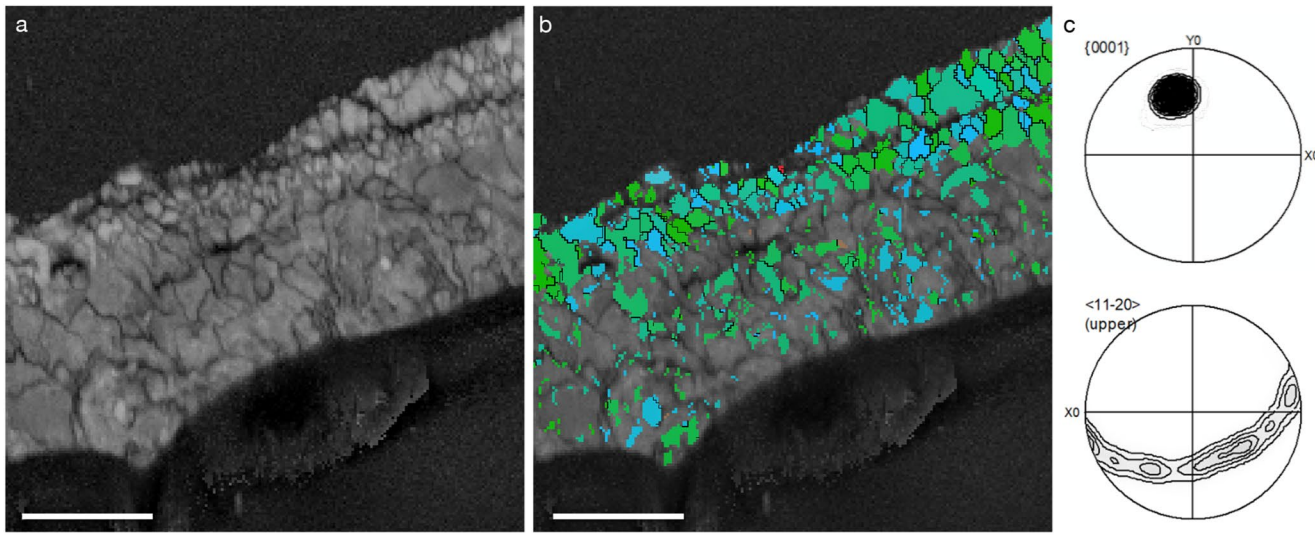

Figure 5. Electron backscatter diffraction image of *G. ruber albus*. (a) Band contrast image and (b) indexed calcite, colored according to the crystallographic orientation using the Euler angle coloring. Those that are not colored could not be successfully indexed as calcite. Grain boundaries are assigned for a misorientation >10°. (c) Crystallographic orientations are indicated in upper hemisphere pole figures, for the *c*-axis (upper pole figure, {0001}) and *a*-axis (lower pole figure, {11–20}), for one point per grain, showing a strong alignment of the *c*-axis and random orientation of the *a*-axis perpendicular to the *c*-axis. The scale bar is 10 μm in both images.

crystalline accessory phases such as vaterite at amounts of >3% as reported by Jacob et al. (2017), are expected to be detectable. The lack of vaterite in samples of the low-Mg calcite species *G. ruber albus* could be attributed (a) to possible recrystallization in cold formalin solution before picking, (b) vaterite not always being formed and/or retained in hyaline low-Mg calcite foraminifer tests, or (c) the presence of vaterite as a nanocrystalline phase, which would not easily be detectable with laboratory XRD setups at the small sample size used in this study. In contrast, a general absence of vaterite in the high-Mg calcite species *A. lessonii* and *O. ammonoides* may be expected, as the formation of vaterite in seawater has only been observed in solutions with low Mg/Ca (Bots et al., 2011). This is valid under the assumption that the Mg/Ca of the ion pool present at their calcification site is generally higher than for low-Mg calcite forming species (Evans et al., 2018), and that Mg/Ca does exhibit influence on polymorph selection in foraminiferal biomineralization. While the absence of metastable vaterite in freshly collected planktic foraminifers disagrees with the results of Jacob et al. (2017), our findings do not preclude the presence of metastable carbonates as precursor or transitional phases, which may be directly involved in the biomineralization process of the shell on short time scales.

In freshly sampled *A. lessonii* and *O. ammonoides*, an amorphous background is observed, which could either be caused by amorphous or nanocrystalline $CaCO_3$ phases, or residues of organic cell material, which cannot be distinguished based on the present data (Figure 2a). For the freshly collected specimens of *G. ruber albus*, the presence or absence of amorphous content cannot be confirmed based on the present analyses. An amorphous background signal that could be attributed to amorphous or nanocrystalline material is not present in samples collected from sediment surfaces. While we were unable to unambiguously detect vaterite or ACC in these foraminifers, this may not be surprising. As calcite is substantially more stable than stabilized amorphous material, a biologically controlled mechanism allowing for fast transformation of an amorphous precursor material means that the preservation of large quantities of ACC in the shell is unlikely.

4.2. Crystallographic Structure of Foraminiferal Test Calcite

The crystallographic structure of foraminifer test calcite is similar for the investigated species within the categories of hyaline low-Mg calcite and hyaline high-Mg calcite, corresponding to likely broadly similar biomineralization mechanisms present within these groups (Bentov & Erez, 2006; de Nooijer et al., 2014; Evans et al., 2018). Among the investigated cations, Mg^{2+} and Sr^{2+} are expected to notably impact the crystal structure due to a difference in the M^{2+}-CO_3^{2-} bond distances, as they are known to be incorporated in the calcite lattice as

substituents of Ca^{2+} (Nielsen et al., 2013; Paquette & Reeder, 1990; Yoshimura et al., 2017). From a comparison of the measured changes in unit cell parameters with the measured Mg/Ca of the shells of 3–150 mmol mol^{-1} (Table 1), it becomes apparent that the foraminifer test Mg/Ca is the dominant controlling parameter of crystallographic changes.

Sodium is present at approximately 6–8 mmol mol^{-1} in all shells of the low-Mg foraminifers (Figure 1), and could contribute to the crystallographic structure of foraminiferal calcite due to the necessity of creating defects along with the incorporation of monovalent ions (Ishikawa & Ichikuni, 1984; Yoshimura et al., 2017). However, as Na^+ and Ca^{2+} have similar bond lengths in carbonates, a deviation of lattice parameters other than a reduction of symmetry is not expected with Na^+ incorporation (Yoshimura et al., 2017). Moreover, preferred leaching of Na^+ from foraminiferal calcite indicates a chemical environment resembling organic-rich and disordered phases in planktic foraminifers (Yoshimura et al., 2017), which means that some of the measured sodium is likely to be located in inter-crystallite rims or associated with organics rather than in crystalline calcite. Hence, coupled with its low concentration, the contribution of Na^+ to the crystallographic structure of foraminifers is negligible.

For *C. wuellerstorfi*, the foraminiferal calcite is observed to exhibit significantly larger unit cell dimensions than geological calcite (Table 1), which can be attributed to lattice distortions caused by strain and defects. Lattice distortions are likely introduced to the crystal lattice by occluded organic material, which has been observed for other biominerals and reproduced in experimentally precipitated carbonates (Borukhin et al., 2012; Kim et al., 2011; Kontrec et al., 2004; Lang et al., 2020; Pokroy et al., 2004, 2006; Rae Cho et al., 2016; Seknazi & Pokroy, 2018; Zolotoyabko, 2017). The generation of internal strain and stress due to the presence of impurities seems to be a widespread mechanism in biominerals, as the organism benefits from mechanical advantages such as enhanced toughness and fracture-resistance (Pokroy et al., 2004; Polishchuk et al., 2017; Seknazi & Pokroy, 2018; Wolf et al., 2016; Wolf, 2021). Our observations indicate that this is the case in some foraminifer species as well, which should be confirmed by systematic high-resolution synchrotron studies.

In the pair distribution function (PDF), calculated from 1D bulk XRD measurements, different shapes and intensities are observed for individual signals at small interatomic distances <20 Å between low-Mg and high-Mg calcite forming species (Figure 3a). The difference in shape is present, for example, in signals at 3.1–3.2 Å (Ca-C) and 3.9–4.4 (Ca-Ca), which is consistent with a contraction of the lattice due to the partial replacement of Ca^{2+} for Mg^{2+}. This is in agreement with the coordination environment of Mg^{2+} in foraminiferal calcite by Near-Edge X-ray Absorption Fine Structure as uniformly octahedrally coordinated, and hence substituting for Ca^{2+} in the calcite lattice (Branson et al., 2013). The difference observed for high-Mg calcite species in the 4.0–4.2 Å signal (Figure 3a), which includes Ca-Ca interactions in direction of the *c*-axis, might indicate a preferential incorporation of Mg^{2+} in direction of the c-axis of foraminifer test calcite, as also observed in other biogenic calcites (Graf, 1961; Zolotoyabko et al., 2010). The additional signal at 1.6 Å present for the high-Mg calcite benthic species (Figure 3a) is likely caused by Mg-O distances as well as artifacts of the Fourier transformation.

4.3. Crystallite Size Determination by Rietveld and PDF

The crystallite size determination for hyaline low-Mg planktic and high-Mg benthic foraminifers based on Rietveld refinement yields values between 70 and 85 nm (Table 1, Figure 2d), which is in agreement with the ordering length (300–500 Å; 30–50 nm) we observed in the PDF (Table 1, Figure 3b). The refined crystallite domain sizes of the different hyaline foraminifer species are similar, except for *C. wuellerstorfi*, which exhibits an average crystallite size that is approximately two times that of the other investigated species (Table 1, Figure 2). This indicates that the general construction of the test might be similar within low-Mg planktic and high-Mg benthic foraminifers, but cannot be assumed to be identical for all hyaline species. For crystalline materials with domain sizes as large as tens of nanometers, laboratory-based PDF analysis can serve as an unequivocal measure only for the minimum ordering length, due to instrumental dampening and artifacts of the Fourier transformation (Egami & Billinge, 2003), which is why this discrepancy is not resolved here. Our findings are consistent with crystallite dimension of 20–50 nm found in TEM studies of few investigated planktic and benthic foraminifers (Jacob et al., 2017; Oaki et al., 2006), and are within a similar range as a coherence length of 110–160 nm for the benthic foraminifer *Patellina*, as determined by high-resolution synchrotron-based XRD (Berman et al., 1993).

The XRD measurements in this study were conducted on assemblages of whole foraminifer tests, which contain different materials such as ontogenetic calcite, encrustations, residues of spines, and possibly partially

recrystallized material (cf. Figure S1 in Supporting Information S1). These different calcite phases exhibit different morphologies, are formed by different mechanisms, result in different M/Ca compositions, and are hence expected to differ in crystallographic aspects (Izumida et al., 2022; Schiebel & Hemleben, 2017). However, only one dominant crystalline Mg-calcite phase is visible in the diffraction patterns of the hyaline foraminifers (Figures 2a and 2b). Hence, the relative volume of alternative phases can be concluded to be small in comparison to the bulk wall material, and may qualitatively not interfere with results from refinements and PDF calculations (i.e., only the spine base remains present in the test wall, see Figure S1 in Supporting Information S1, and additional nanoparticulate phases are not resolved). In addition, element concentrations are highly heterogeneous in the bulk shell material on a micrometer scale (e.g., in bandings in some species, possibly in association with organic material), may differ between chambers, and vary with the ontogenetic stages of the individuals as shown for several species (Branson et al., 2015, 2016; Eggins et al., 2003; Erez, 2003; Fehrenbacher et al., 2017; Geerken et al., 2019, 2022; Khanolkar et al., 2021; Schiebel & Hemleben, 2017; Yoshimura et al., 2017). As heterogeneous element concentrations are likely to cause heterogeneous levels of incorporation of impurities into the foraminifer test calcite lattice, it is possible that different grains experience different concentrations of defects. Considering all of the above, our determination of foraminifer test calcite structural parameters and crystallite dimensions represent a good estimate of the dominant shell wall component.

4.4. Nanogranular Fracture Surfaces

Scanning electron microscopy images of fractured hyaline foraminifer tests show a nanogranular substructure of the chamber walls in both planktic and benthic species (50–150 nm rounded entities, Figure 4). This is different from the smooth cleavage planes that would be expected when fracturing a single crystal, and also different from an apparently random assemblage of crystal needles of the miliolid species (Figure 4). As the chambers were fractured mechanically and without any chemical treatment, the observed morphology may be created by fracture propagation along the weakest part of the material, which are nanometer sized grain boundaries (Seto et al., 2012; Wolf et al., 2016). This implies that hyaline foraminifer bulk chamber walls are composed of at least two distinct materials, that are calcite nanocrystallites and a separate inter-crystallite material, which may differ in composition and/or chemical properties.

Nanogranular features in fracture surfaces of foraminifer chamber walls are observed in this study for hyaline foraminifers, which were either live-collected, or selected from surface sediment assemblages (Figure 4, approx. age 0–3 ka). The similarity of the texture of live (plankton tow), core-top, and fossil planktic foraminifers, as observed in this and many studies (e.g., Debenay et al., 1996; Dubicka et al., 2018; Edgar et al., 2015; Nagai, Uematsu, Chen, et al., 2018; Nagai, Uematsu, Wani, et al., 2018; Pearson et al., 2001; Schiebel & Hemleben, 2017; Sexton et al., 2006), demonstrates that the nanogranular texture can be readily preserved in empty tests. Disintegration of an energetically stabilized crystal, which may have been produced by dissolution/recrystallization during diagenesis, into densely packed nanometer-sized crystallites under conditions present in marine surface sediments is considered unlikely. For example, in some cases, fossil foraminifers known to have undergone partial recrystallization have been shown to be partly composed of much larger (rather than smaller) crystallites than the pristine modern samples utilized here (Kozdon et al., 2011). Hence, we argue that the nanogranular features observed here are representative of the original test structure. In other cases, it has been observed that nanogranular structures can be present in fossils where geochemical data suggests diagenetic recrystallization has occurred (Edgar et al., 2015; Sexton et al., 2006). We suggest that this implies a highly localized diagenetic dissolution/recrystallization reaction of the crystallites, or their surface, rather than complete dissolution/recrystallization of the whole chamber wall. This could, for example, be facilitated by a confinement of the crystallites by a rim of organic and/or impurity rich material (Bergström et al., 2015; Brunner et al., 2020; Sommerdijk & de With, 2008; Wolf et al., 2016), supporting our inferences on shell microstructure given above.

4.5. Micrometer Sized Regions of Coherent Scattering

The EBSD map of the hyaline planktic foraminifer *G. ruber albus* shows 3–10 μm sized regions of coherent crystallographic orientation to be strongly aligned with the *c*-axis oriented perpendicular to the chamber surface (Figure 5). This organization seems to be a common principle observed in a variety of planktic and benthic foraminifers, with similar reports of grain sizes for planktic (∼10 μm) and benthic (∼20 μm) species (Pabich et al., 2020; Read, 2019; Yin et al., 2021). The strict crystallographic orientation of the test calcite *c*-axes is

thought to reflect the presence of a tightly controlled, biochemically-governed mechanism in hyaline foraminifers, which is facilitated by epitaxial crystallisation on organic templates (Ní Fhlaithearta et al., 2013; Towe & Cifelli, 1967; Weiner & Erez, 1984). The presence of distinct crystals rather than one continuously aligned entity is indicated by randomly oriented *a*-axes (Figure 5), which suggests that foraminiferal test formation is a discontinuous process, that directs crystallisation into different compartments, possibly by the presence of separating organic sheets (Nagai, Uematsu, Chen, et al., 2018; Nakajima et al., 2016; Tyszka et al., 2019). A strict direction of the crystallographic *c*-axis perpendicular to the shell surface has also been observed in other biominerals and has been suggested to serve mechanical as well as optical purposes (Gim et al., 2019; Harding et al., 2014; Jacob et al., 2017; Merkel et al., 2009; Sommerdijk & de With, 2008; Towe & Cifelli, 1967; Wolf, 2021; Wolf et al., 2016).

4.6. Mesocrystals and Non-Classical Crystal Growth in Hyaline Foraminifer Tests

A grain size of several micrometers observed via EBSD, together with a crystallite domain size of up to ∼100 nm as determined from diffraction experiments and SEM images, indicates that hyaline foraminifer chamber walls are mostly made of micrometer scale mesocrystals (Figures 2–5). Mesocrystals are constituted of distinguishable nanometer scale entities, which are crystallographically aligned in a superlattice, and hence display crystallographic properties similar to single crystals at the larger scale (Bergström et al., 2015; Cölfen & Antonietti, 2005; Kim et al., 2014; Seto et al., 2012; Sturm & Cölfen, 2016). As we show in this study, these criteria are met by hyaline foraminiferal test calcites, which entails the necessity of considering chemical principles of mesocrystal formation for foraminiferal biomineralization models.

In biominerals as well as in experimental studies, mesocrystallisation has been proposed to be realized via a non-classical crystal growth mechanism, that is, attachment of nanoparticles to a growing crystal surface, in contrast to classical growth by single ions (Bergström et al., 2015; Cölfen & Antonietti, 2005; De Yoreo et al., 2015; Floquet & Vielzeuf, 2012; Gal et al., 2014; Jehannin et al., 2019; Rao & Cölfen, 2017; Sturm & Cölfen, 2016). These nanoparticles can either be nanocrystals, which attach in an oriented manner (oriented attachment), or metastable (amorphous, colloidal or liquid) phases, which crystallize upon interaction with the mineral surface (Bergström et al., 2015; De Yoreo et al., 2015; Gal et al., 2014; Huang et al., 2018; Rao & Cölfen, 2018; Rodríguez-Navarro et al., 2016; Seto et al., 2012; Sturm & Cölfen, 2016; Wolf, 2021). The presence of a non-classical mechanism resulting in a mesocrystal can mean that the final average crystallite domain size does not exceed the size of the attaching unit, which we confirm for hyaline foraminiferal test calcite by XRD methods (crystallite domain sizes range nanometer dimensions, Table 1, Figures 2 and 3; as well as Berman et al., 1993). At the same time, the lattice orientation remains the same between different nanocrystallites of the same mesocrystal, which results in diffraction patterns similar to single crystals for each distinct mesocrystal, visible as, for example, spots instead of rings in XRD (Bergström et al., 2015; Cölfen & Antonietti, 2005; Gal et al., 2014; Jehannin et al., 2019; Sturm & Cölfen, 2016). This is confirmed for hyaline foraminiferal calcite by EBSD (micrometer-sized regions of coherent crystallographic orientation, Figure 5; and Pabich et al., 2020; Read, 2019; Yin et al., 2021).

Crystallographic orientation and/or formation of the nanoparticles within the mesocrystals has been suggested to be achieved (a) by epitaxial crystallisation through mineral bridging, (b) with the guidance of a meshwork of organics, (c) by nucleation of ACC within an organic network and in situ crystallisation, (d) by oriented attachment of a previously formed nanocrystal, (e) by interface-driven nucleation, (f) *via* a polymer-induced liquid precursor (PILP), or (g) by accretion and crystallisation of amorphous colloids (Bergström et al., 2015; Cölfen & Antonietti, 2005; De Yoreo et al., 2015; Jehannin et al., 2019; Oaki et al., 2006; Pouget et al., 2009; Rao & Cölfen, 2017; Rao et al., 2019; Rodríguez-Navarro et al., 2016; Seto et al., 2012; Sommerdijk & de With, 2008; Sturm & Cölfen, 2016; Wolf, 2021; Wolf et al., 2016, 2012; Zhu et al., 2021). Either of these mechanisms may have different implications for the formation of geochemical signals in foraminiferal shell calcite, as they might employ transitional carbonate phases such as ACC and phase transformations to thermodynamically stable calcite, which have the potential to exert control over the evolution of element distributions during test formation (Dietzel et al., 2020; Evans et al., 2020; Mavromatis et al., 2017).

In order to stabilize nanoparticles against growth and prevent the fusion of mesocrystals into a single crystal (devoid of distinguishable building units), organic matter can act as a surfactant or confining matrix, which separates nucleating nanoparticles and prevents coalescence (Bergström et al., 2015; Cölfen & Antonietti, 2005;

Jehannin et al., 2019; Oaki et al., 2006; Rao & Cölfen, 2017; Sturm & Cölfen, 2016). This is consistent with a spherical and irregular shape of the nanocrystals devoid of crystal facets observed in hyaline foraminiferal calcite (Figure 4), which suggests preservation of the initial nanoparticle dimension upon crystallisation. Further confinement of the nanocrystallite might be provided by the formation of a grain boundary of organic matter and/or inorganic impurities during propagation of a crystallisation front within the nanogranule, as observed or proposed for abiogenic and biogenic calcites in the presence and absence of organic matter (Cölfen & Antonietti, 2005; Huang et al., 2018; Jehannin et al., 2019; Oaki et al., 2006; Rao & Cölfen, 2017; Sommerdijk & de With, 2008; Wolf et al., 2016; Wolf, 2021). A distinct inter-crystallite amorphous phase has been observed at grain boundaries in different hyaline foraminifer species in TEM studies from focused ion beam milled wedges of foraminifer shells (Jacob et al., 2017), which could possibly be a stabilized amorphous carbonate-organic composite material (Seto et al., 2012; Wolf et al., 2012, 2016).

Organic matter comprising different proteins and polysaccharides is known to be present at the site of biomineralization and within foraminifer test calcite in both hyaline benthic and planktic species (Cuif et al., 2008; Nagai, Uematsu, Chen, et al., 2018; Ní Fhlaithearta et al., 2013; Robbins & Brew, 1990; Robbins & Donachy, 1991; Sabbatini et al., 2014; Weiner & Erez, 1984). While the spatial distribution of this organic matter with respect to the mesocrystals is unclear, it is known from investigation of (e.g.) the $\delta^{15}N$ proxy that a share of N-containing matter is present in fossil shells even after rigorous cleaning protocols (e.g., Knapp et al., 2005). This implies that a portion of the organic matter is strongly protected within the shell, for which the interior of the mesocrystal is a plausible environment, both in between and within the nanocrystallites (cf. Section 4.2). Hence, it is hypothesized that occlusion of organic matter necessarily happens before or at crystallisation, which would consequently be either during formation of a carbonate phase in contact with organic matter or during nanoparticle attachment and final assembly of the mesocrystal.

Further, it is plausible that the processes outlined above take place in a delimited biomineralization space of a few micrometers width (Erez, 2003; Nagai, Uematsu, Chen, et al., 2018; Tyszka et al., 2019). Confinement of a crystallizing system to a small volume profoundly impacts critical properties such as nucleation dynamics, polymorph selection, and can dictate shape and crystallographic orientation, which is relevant for foraminiferal biomineralization at both the nano- and mesoscale (see Meldrum and O'Shaughnessy (2020) and references within). As such, the three-dimensional structure of the growing mesocrystals as well as their geochemistry are likely to be influenced by this aspect as well.

4.7. Model Extension of Foraminifer Chamber Crystallisation Including Non-Classical Formation Mechanisms

Based on the similarity of features observed for different planktic and benthic species in this study, which cover a wide range of symbiont-barren and symbiont-bearing species consisting of low-Mg and high-Mg calcite (Schiebel & Hemleben, 2017), we hypothesize that the presence of mesocrystalline chamber walls is a common feature of the hyaline foraminifers. Following the evidence given above, we extend the existing hyaline foraminifer biomineralization models (e.g., Bentov & Erez, 2006; Bentov et al., 2009; de Nooijer et al., 2014; Erez, 2003; Evans et al., 2018; Nehrke et al., 2013) by including a step of tightly controlled non-classical mesocrystallisation. We theorize that during formation of the test wall, growth of the mesocrystal can be facilitated by non-classical addition of either a previously formed nanoparticulate metastable carbonate phase, or by in situ formation of such a phase in the vicinity of a previously existing growth front. This model and its implications tie into the following existing key observations for foraminiferal biomineralization:

1. The preservation of a nanogranular fracture surface and nanocrystalline coherence lengths suggest that the nanocrystalline entities generally reflect the dimensions of the units which initially contributed to the growth of the mesocrystal. These dimensions are consistent with ACC precipitated in seawater-like inorganic experimental model solutions, which could serve as an initial precursor phase (Evans et al., 2019).
2. The alignment of the mesocrystal *c*-axis toward the chamber surface suggests that the final crystallisation of the nanoparticular units happens at or after a step of attachment, possibly in direct interaction with an organic template.
3. The presence of organic material within the mesocrystals implies that either formation of a distinct carbonate phase or nanoparticle assembly to the mesocrystal happens within, or in contact with, an organic matrix which possibly plays a role in guiding the final stage of crystallisation (Sturm & Cölfen, 2016; Wolf et al., 2016).

This is consistent with a chamber precipitation template or delimited biomineralization space formed by a meshwork of organic linings (Cuif et al., 2008; Erez, 2003; Frontalini et al., 2019; Nagai, Uematsu, Chen, et al., 2018; Tyszka et al., 2019; Weiner & Erez, 1984).

4. As non-membrane-permeable dyes from labeled seawater are included into the ontogenetic calcite, either formation of the solid nanoparticulate (metastable) carbonate phase or mesocrystal assembly must happen in direct contact with endocytosed seawater (Erez, 2003; Bentov et al., 2009; Evans et al., 2018).

5. Conclusions

Here, we infer aspects of the biomineralization mechanisms of hyaline foraminifers from data generated using diffraction-based methods and electron microscopy, targeting the morphological and crystallographic structure of the foraminiferal test. We find that hyaline foraminifer tests are characterized by the presence of nanocrystallites with a diameter of ∼100 nm, which build mesocrystals of approximately 3–10 µm strictly oriented with their crystallographic *c*-axis perpendicular to the outer test surface. The presence of mesocrystals may imply test formation via non-classical attachment of nanoparticular units in the hyaline foraminifer species analyzed here. Consequently, we propose an extension of existing models of hyaline foraminifer biomineralization, which includes formation of metastable nanoparticular carbonate phases in a delimited biomineralization space, construction of a mesocrystal by non-classical attachment, and directed in situ crystallisation of the mesocrystal. Together with observational evidence on organic linings in foraminifer biomineralization (Branson et al., 2016; Nagai, Uematsu, Chen, et al., 2018; Tyszka et al., 2019), these processes are likely supported or directed by organic compounds and/or templates.

As evidence for such mechanisms have been observed in different hyaline foraminifers in this and previous studies, including planktic and benthic species, symbiont-barren and symbiont bearing species consisting of low-Mg and high-Mg calcite phases, non-classical mesocrystal growth mechanism of tests may be a general feature of hyaline foraminifer test formation. Further understanding of the impact of such a mechanism in foraminiferal biomineralization on proxy formation has the potential to decrease uncertainties arising from "vital effects", and hence contribute to more accurate and precise paleoenvironmental information.

Data Availability Statement

The data obtained for this research is available at https://doi.org/10.17617/3.D7HN3I (Arns et al., 2022).

Acknowledgments
We thank Ulrike Weis and Brigitte Stoll (MPIC) for conducting the LA-ICP-MS measurements, and Antje Sorowka (MPIC) for SEM imaging. We are grateful to Michael Steiert (MPIP) for performing XRD measurements. Further, we would like to thank two anonymous reviewers for thoughtful and constructive comments which improved this manuscript. Open Access funding enabled and organized by Projekt DEAL.

References

Addadi, L., Raz, S., & Weiner, S. (2003). Taking advantage of disorder: Amorphous calcium carbonate and its roles in biomineralization. *Advanced Materials*, *15*(12), 959–970. https://doi.org/10.1002/adma.200300381

Allen, K. A., Hönisch, B., Eggins, S. M., Haynes, L. L., Rosenthal, Y., & Yu, J. (2016). Trace element proxies for surface ocean conditions: A synthesis of culture calibrations with planktic foraminifera. *Geochimica et Cosmochimica Acta*, *193*, 197–221. https://doi.org/10.1016/j.gca.2016.08.015

Arns, A. I., Evans, D., Schiebel, R., Fink, L., Mezger, M., Alig, E., et al. (2022). Mesocrystalline architecture in hyaline foraminifer shells indicates a non-classical crystallization pathway [Data set]. *Edmond*. https://doi.org/10.17617/3.D7HN3I

Bé, A. W. H., Hemleben, C., Anderson, O. R., Spindler, M., & Be, A. W. H. (1979). Chamber formation in planktonic foraminifera. *Micropaleontology*, *25*(3), 294. https://doi.org/10.2307/1485304

Bentov, S., Brownlee, C., & Erez, J. (2009). The role of seawater endocytosis in the biomineralization process in calcareous foraminifera. *Proceedings of the National Academy of Sciences of the United States of America*, *106*(51), 21500–21504. https://doi.org/10.1073/pnas.0906636106

Bentov, S., & Erez, J. (2006). Impact of biomineralization processes on the Mg content of foraminiferal shells: A biological perspective. *Geochemistry, Geophysics, Geosystems*, *7*(1). https://doi.org/10.1029/2005GC001015

Bergström, L., Sturm (née Rosseeva), E. V., Salazar-Alvarez, G., & Cölfen, H. (2015). Mesocrystals in biominerals and colloidal arrays. *Accounts of Chemical Research*, *48*(5), 1391–1402. https://doi.org/10.1021/ar500440b

Berman, A., Hanson, J., Leiserowitz, L., Koetzle, T. F., Weiner, S., & Addadi, L. (1993). Biological control of crystal texture: A widespread strategy for adapting crystal properties to function. *Science*, *259*(5096), 776–779. https://doi.org/10.1126/science.259.5096.776

Berthold, W.-U. (1976). Biomineralisation bei milioliden Foraminiferen und die Matritzen-Hypothese. *Naturwissenschaften*, *63*(4), 196–197. https://doi.org/10.1007/bf00624226

Blackmon, P. D., & Todd, R. (1959). Mineralogy of some foraminifera as related to their classification and ecology. *Journal of Paleontology*, *33*(1), 1–15. https://doi.org/10.2307/1300802

Borukhin, S., Bloch, L., Radlauer, T., Hill, A. H., Fitch, A. N., & Pokroy, B. (2012). Screening the incorporation of amino acids into an inorganic crystalline host: The case of calcite. *Advanced Functional Materials*, *22*(20), 4216–4224. https://doi.org/10.1002/adfm.201201079

Bots, P., Benning, L. G., Rickaby, R. E. M., & Shaw, S. (2011). The role of SO_4 in the switch from calcite to aragonite seas. *Geology*, *39*(4), 331–334. https://doi.org/10.1130/G31619.1

Bots, P., Benning, L. G., Rodriguez-Blanco, J.-D., Roncal-Herrero, T., & Shaw, S. (2012). Mechanistic Insights into the crystallization of amorphous calcium carbonate (ACC). *Crystal Growth & Design*, *12*(7), 3806–3814. https://doi.org/10.1021/cg300676b

Branson, O., Bonnin, E. A., Perea, D. E., Spero, H. J., Zhu, Z., Winters, M., et al. (2016). Nanometer-scale chemistry of a calcite biomineralization template: Implications for Skeletal composition and nucleation. *Proceedings of the National Academy of Sciences*, *113*(46), 12934–12939. https://doi.org/10.1073/pnas.1522864113

Branson, O., Kaczmarek, K., Redfern, S. A. T., Misra, S., Langer, G., Tyliszczak, T., et al. (2015). The coordination and distribution of B in foraminiferal calcite. *Earth and Planetary Science Letters*, *416*, 67–72. https://doi.org/10.1016/j.epsl.2015.02.006

Branson, O., Redfern, S. A. T., Tyliszczak, T., Sadekov, A., Langer, G., Kimoto, K., & Elderfield, H. (2013). The coordination of Mg in foraminiferal calcite. *Earth and Planetary Science Letters*, *383*,134–141. https://doi.org/10.1016/j.epsl.2013.09.037

Brunner, J., Maier, B., Rosenberg, R., Sturm, S., Cölfen, H., & Sturm, E. V. (2020). Nonclassical Recrystallization. *Chemistry - A European Journal*, *26*(66), 15242–15248. https://doi.org/10.1002/chem.202002873

Coelho, A. A. (2016a). *TOPAS-Academic*. Version 6: Technical Reference, 208. Retrieved from http://www.bruker-axs.de/

Coelho, A. A. (2016b). *TOPAS-Academic V6*. Coelho Software.

Cölfen, H., & Antonietti, M. (2005). Mesocrystals: Inorganic superstructures made by highly parallel crystallization and controlled alignment. *Angewandte Chemie International Edition*, *44*(35), 5576–5591. https://doi.org/10.1002/anie.200500496

Cuif, J. P., Dauphin, Y., Farre, B., Nehrke, G., Nouet, J., & Salomé, M. (2008). Distribution of sulphated polysaccharides within calcareous biominerals suggests a widely shared two-step crystallization process for the microstructural growth units. *Mineralogical Magazine*, *72*(1), 233–237. https://doi.org/10.1180/minmag.2008.072.1.233

Debenay, J., Guillou, J., Geslin, E., & Lesourd, M. (2000). Crystallization of calcite in foraminiferal tests. *Micropaleontology*, *46*, 87–94.

Debenay, J. P., Guillou, J. J., & Lesourd, M. (1996). Colloidal calcite in foraminiferal tests; crystallization and texture of the test. *The Journal of Foraminiferal Research*, *26*(4), 277–288. https://doi.org/10.2113/gsjfr.26.4.277

deNooijer, L. J., Spero, H. J., Erez, J., Bijma, J., & Reichart, G. J. (2014). Biomineralization in perforate foraminifera. *Earth-Science Reviews*, *135*, 48–58. https://doi.org/10.1016/j.earscirev.2014.03.013

deNooijer, L. J., Toyofuku, T., & Kitazato, H. (2009). Foraminifera promote calcification by elevating their intracellular pH. *Proceedings of the National Academy of Sciences*, *106*(36), 15374–15378. https://doi.org/10.1073/pnas.0904306106

De Villiers, J. P. R. (1971). Crystal structures of aragonite, strontianite, and witherite. *American Mineralogist*, *56*, 758–767. Retrieved from http://www.minsocam.org/ammin/AM56/AM56_758.pdf

De Yoreo, J. J., Gilbert, P., Sommerdijk, N. A. J. M., Penn, R. L., Whitelam, S., Joester, D., et al. (2015). Crystallization by particle attachment in synthetic, biogenic, and geologic environments. *Science*, *349*(6247), aaa6760. https://doi.org/10.1126/science.aaa6760

Dietzel, M., Purgstaller, B., Kluge, T., Leis, A., & Mavromatis, V. (2020). Oxygen and clumped isotope fractionation during the formation of Mg calcite via an amorphous precursor. *Geochimica et Cosmochimica Acta*, *276*, 258–273. https://doi.org/10.1016/j.gca.2020.02.032

Dubicka, Z., Owocki, K., & Gloc, M. (2018). Micro- and nanostructures of calcareous foraminiferal tests: Insight from representatives of Miliolida, Rotaliida and Lagenida. *Journal of Foraminiferal Research*, *48*(2), 142–155. https://doi.org/10.2113/gsjfr.48.2.142

Edgar, K. M., Anagnostou, E., Pearson, P. N., & Foster, G. L. (2015). Assessing the impact of diagenesis on δ11B, δ13C, δ18O, Sr/Ca and B/Ca values in fossil planktic foraminiferal calcite. *Geochimica et Cosmochimica Acta*, *166*, 189–209. https://doi.org/10.1016/j.gca.2015.06.018

Egami, T., & Billinge, S. J. L. (2003). In R. W. Chan (Ed.), *Underneath the Bragg peaks structural analysis of complex materials* (Vol. 6). Pergamon Materuals Series. https://doi.org/10.1016/S1369-7021(03)00635-7

Eggins, S., De Deckker, P., & Marshall, J. (2003). Mg/Ca variation in planktonic foraminifera tests: Implications for reconstructing -palaeo-seawater temperature and habitat migration. *Earth and Planetary Science Letters*, *212*(3–4), 291–306. https://doi.org/10.1016/S0012-821X(03)00283-8

Erez, J. (2003). The source of ions for biomineralization in foraminifera and their implications for paleoceanographic proxies. *Reviews in Mineralogy and Geochemistry*, *54*(1), 115–149. https://doi.org/10.2113/0540115

Evans, D., Gray, W. R., Rae, J. W. B., Greenop, R., Webb, P. B., Penkman, K., et al. (2020). Trace and major element incorporation into amorphous calcium carbonate (ACC) precipitated from seawater. *Geochimica et Cosmochimica Acta*, *290*, 293–311. https://doi.org/10.1016/j.gca.2020.08.034

Evans, D., & Müller, W. (2018). Automated extraction of a five-year LA-ICP-MS trace element data set of ten common glass and carbonate reference materials: Long-term data quality, optimisation and laser cell homogeneity. *Geostandards and Geoanalytical Research*, *42*(2), 159–188. https://doi.org/10.1111/ggr.12204

Evans, D., Müller, W., & Erez, J. (2018). Assessing foraminifera biomineralisation models through trace element data of cultures under variable seawater chemistry. *Geochimica et Cosmochimica Acta*, *236*, 198–217. https://doi.org/10.1016/j.gca.2018.02.048

Evans, D., Müller, W., Oron, S., & Renema, W. (2013). Eocene seasonality and seawater alkaline Earth reconstruction using shallow-dwelling large benthic foraminifera. *Earth and Planetary Science Letters*, *381*, 104–115. https://doi.org/10.1016/j.epsl.2013.08.035

Evans, D., Webb, P. B., Penkman, K., Kröger, R., & Allison, N. (2019). The characteristics and biological relevance of inorganic amorphous calcium carbonate (ACC) precipitated from seawater. *Crystal Growth & Design*, *19*(8), 4300–4313. https://doi.org/10.1021/acs.cgd.9b00003

Fehrenbacher, J. S., Russell, A. D., Davis, C. V., Gagnon, A. C., Spero, H. J., Cliff, J. B., et al. (2017). Link between light-triggered Mg-banding and chamber formation in the planktic foraminifera Neogloboquadrina dutertrei. *Nature Communications*, *8*(1), 15441. https://doi.org/10.1038/ncomms15441

Fischer, G., & Wefer, G. (Eds.). (1999). *Use of proxies in paleoceanography*. Springer Berlin Heidelberg. https://doi.org/10.1007/978-3-642-58646-0

Floquet, N., & Vielzeuf, D. (2012). Ordered misorientations and preferential directions of growth in mesocrystalline red coral sclerites. *Crystal Growth & Design*, *12*(10), 4805–4820. https://doi.org/10.1021/cg300528h

Frontalini, F., Losada, M. T., Toyofuku, T., Tyszka, J., Goleń, J., deNooijer, L., et al. (2019). Foraminiferal ultrastructure: A perspective from fluorescent and fluorogenic probes. *Journal of Geophysical Research: Biogeosciences*, *124*(9), 2823–2850. https://doi.org/10.1029/2019JG005113

Gal, A., Kahil, K., Vidavsky, N., DeVol, R. T., Gilbert, P., Fratzl, P., et al. (2014). Particle accretion mechanism underlies biological crystal growth from an amorphous precursor phase. *Advanced Functional Materials*, *24*(34), 5420–5426. https://doi.org/10.1002/adfm.201400676

Geerken, E., deNooijer, L., Toyofuku, T., Roepert, A., Middelburg, J. J., Kienhuis, M. V. M., et al. (2022). High precipitation rates characterize biomineralization in the benthic foraminifer Ammonia beccarii. *Geochimica et Cosmochimica Acta*, *318*, 70–82. https://doi.org/10.1016/j.gca.2021.11.026

Geerken, E., deNooijer, L. J., Roepert, A., Polerecky, L., King, H. E., & Reichart, G. J. (2019). Element banding and organic linings within chamber walls of two benthic foraminifera. *Scientific Reports*, *9*(1), 3598. https://doi.org/10.1038/s41598-019-40298-y

Gim, J., Schnitzer, N., Otter, L. M., Cui, Y., Motreuil, S., Marin, F., et al. (2019). Nanoscale deformation mechanics reveal resilience in nacre of Pinna Nobilis shell. *Nature Communications*, *10*(1), 1–8. https://doi.org/10.1038/s41467-019-12743-z

Graf, D. L. (1961). Crystallographic tables for the rhombohedral carbonates. *American Mineralogist*, *46*, 1283–1316.

Harding, J. H., Freeman, C. L., & Duffy, D. M. (2014). Oriented crystal growth on organic monolayers. *CrystEngComm*, *16*(8), 1430–1438. https://doi.org/10.1039/c3ce41677a

Heinrich, C. A., Pettke, T., Halter, W. E., Aigner-Torres, M., Audétat, A., Günther, D., et al. (2003). Quantitative multi-element analysis of minerals, fluid and melt inclusions by laser-ablation inductively-coupled-plasma mass-spectrometry. *Geochimica et Cosmochimica Acta*, *67*(18), 3473–3497. https://doi.org/10.1016/S0016-7037(03)00084-X

Hemleben, C., Anderson, O. R., Berthold, W.-U., & Spindler, M. (1986). *Calcification and chamber formation in foraminifera—A brief overview* (pp. 237–249). Biomineralization in Lower Plants and Animals.

Huang, Y. C., Gindele, M. B., Knaus, J., Rao, A., & Gebauer, D. (2018). On mechanisms of mesocrystal formation: Magnesium ions and water environments regulate the crystallization of amorphous minerals. *CrystEngComm*, *20*(31), 4395–4405. https://doi.org/10.1039/c8ce00241j

Ishikawa, M., & Ichikuni, M. (1984). Uptake of sodium and potassium by calcite. *Chemical Geology*, *42*(1–4), 137–146. https://doi.org/10.1016/0009-2541(84)90010-X

Izumida, K., Takasaki, M., Fujimaki, R., Nagai, Y., Oaki, Y., Naito, K., et al. (2022). Characterization of calcite spines of planktonic foraminifers (Globigerinidae). *CrystEngComm*, *24*(13), 2446–2450. https://doi.org/10.1039/D2CE00110A

Jacob, D. E., Wirth, R., Agbaje, O. B. A., Branson, O., & Eggins, S. M. (2017). Planktic foraminifera form their shells via metastable carbonate phases. *Nature Communications*, *8*(1), 1265. https://doi.org/10.1038/s41467-017-00955-0

Jehannin, M., Rao, A., & Cölfen, H. (2019). New horizons of nonclassical crystallization. *Journal of the American Chemical Society*, *141*(26), 10120–10136. https://doi.org/10.1021/jacs.9b01883

Jochum, K. P., Jentzen, A., Schiebel, R., Stoll, B., Weis, U., Leitner, J., et al. (2019). High-resolution Mg/Ca measurements of foraminifer shells using femtosecond LA-ICP-MS for paleoclimate proxy Development. *Geochemistry, Geophysics, Geosystems*, *20*(4), 2053–2063. https://doi.org/10.1029/2018GC008091

Jochum, K. P., Weis, U., Stoll, B., Kuzmin, D., Yang, Q., Raczek, I., et al. (2011). Determination of reference values for NIST SRM 610-617 glasses following ISO guidelines. *Geostandards and Geoanalytical Research*, *35*(4), 397–429. https://doi.org/10.1111/j.1751-908X.2011.00120.x

Juhás, P., Davis, T., Farrow, C. L., & Billinge, S. J. L. (2013). PDFgetX3: A rapid and highly automatable program for processing powder diffraction data into total scattering pair distribution functions. *Journal of Applied Crystallography*, *46*(2), 560–566. https://doi.org/10.1107/S0021889813005190

Katz, M. E., Cramer, B. S., Franzese, A., Hönisch, B., Miller, K. G., Rosenthal, Y., & Wright, J. D. (2010). Traditional and emerging geochemical proxies in foraminifera. *Journal of Foraminiferal Research*, *40*(2), 165–192. https://doi.org/10.2113/gsjfr.40.2.165

Khalifa, G. M., Kirchenbuechler, D., Koifman, N., Kleinerman, O., Talmon, Y., Elbaum, M., et al. (2016). Biomineralization pathways in a foraminifer revealed using a novel correlative cryo-fluorescence–SEM–EDS technique. *Journal of Structural Biology*, *196*(2), 155–163. https://doi.org/10.1016/j.jsb.2016.01.015

Khanolkar, S., Schiebel, R., Singh, A., Saraswati, P. K., Jochum, K. P., Weis, U., et al. (2021). Intra-test variations in trace element composition of Amphistegina lessonii using femtosecond-laser ablation-ICP-mass spectrometry: A field study from Akajima, Okinawa Prefecture, Japan. *Geochemistry, Geophysics, Geosystems*, *22*(3). https://doi.org/10.1029/2020gc009443

Kim, Y.-Y., Ganesan, K., Yang, P., Kulak, A. N., Borukhin, S., Pechook, S., et al. (2011). An artificial biomineral formed by incorporation of copolymer micelles in calcite crystals. *Nature Materials*, *10*(11), 890–896. https://doi.org/10.1038/nmat3103

Kim, Y.-Y., Schenk, A. S., Ihli, J., Kulak, A. N., Hetherington, N. B. J., Tang, C. C., et al. (2014). A critical analysis of calcium carbonate mesocrystals. *Nature Communications*, *5*(1), 4341. https://doi.org/10.1038/ncomms5341

King, K., & Hare, P. E. (1972). Amino acid composition of planktonic foraminifera: A paleobiochemical approach to evolut*ion. Sc*ience, *175*(4029), 1461–1463. https://doi.org/10.1126/science.175.4029.1461

Knapp, A. N., Sigman, D. M., & Lipschultz, F. (2005). N isotopic composition of dissolved organic nitrogen and nitrate at the Bermuda Atlantic time-series Study site. *Global Biogeochemical Cycles*, *19*(1), 1–15. https://doi.org/10.1029/2004GB002320

Konrad, F., Purgstaller, B., Gallien, F., Mavromatis, V., Gane, P., & Dietzel, M. (2018). Influence of aqueous Mg concentration on the transformation of amorphous calcium carbonate. *Journal of Crystal Growth*, *498*, 381–390. https://doi.org/10.1016/j.jcrysgro.2018.07.018

Kontrec, J., Kralj, D., Brečević, L., Falini, G., Fermani, S., Noethig-Laslo, V., & Mirosavljević, K. (2004). Incorporation of inorganic anions in calcite. *European Journal of Inorganic Chemistry*, *23,* 4579–4585. https://doi.org/10.1002/ejic.200400268

Kozdon, R., Kelly, D. C., Kita, N. T., Fournelle, J. H., & Valley, J. W. (2011). Planktonic foraminiferal oxygen isotope analysis by ion microprobe technique suggests warm tropical sea surface temperatures during the Early Paleogene. *Paleoceanography*, *26*(3). https://doi.org/10.1029/2010PA002056

Lang, A., Mijowska, S., Polishchuk, I., Fermani, S., Falini, G., Katsman, A., et al. (2020). Acidic monosaccharides become incorporated into calcite single crystals. *—A European Journal*, *26*(70), 16860–16868. https://doi.org/10.1002/chem.202003344

Langer, M. R. (2008). Assessing the contribution of foraminiferan protists to global ocean carbonate production. *The Journal of Eukaryotic Microbiology*, *55*(3), 163–169. https://doi.org/10.1111/j.1550-7408.2008.00321.x

Loeblich, A. R., & Tappan, H. (1984). Suprageneric classification of the Foraminiferida (Protozoa). *Micropaleontology*, *30*(1), 1. https://doi.org/10.2307/1485456

MacIás-Sánchez, E., Willinger, M. G., Pina, C. M., & Checa, A. G. (2017). Transformation of ACC into aragonite and the origin of the nanogranular structure of nacre. *Scientific Reports*, *7*(1), 1–11. https://doi.org/10.1038/s41598-017-12673-0

Mavromatis, V., Purgstaller, B., Dietzel, M., Buhl, D., Immenhauser, A., & Schott, J. (2017). Impact of amorphous precursor phases on magnesium isotope signatures of Mg-calcite. *Earth and Planetary Science Letters*, *464*, 227–236. https://doi.org/10.1016/j.epsl.2017.01.031

Meldrum, F. C., & O'Shaughnessy, C. (2020). Crystallization in confinement. *Advanced Materials*, *32*(31), 2001068. https://doi.org/10.1002/adma.202001068

Merkel, C., Deuschle, J., Griesshaber, E., Enders, S., Steinhauser, E., Hochleitner, R., et al. (2009). Mechanical properties of modern calcite-(Mergerlia Truncata) and phosphate-shelled brachiopods (Discradisca Stella and Lingula Anatina) determined by nanoindentation. *Journal of Structural Biology*, *168*(3), 396–408. https://doi.org/10.1016/j.jsb.2009.08.014

Morard, R., Füllberg, A., Brummer, G. J. A., Greco, M., Jonkers, L., Wizemann, A., et al. (2019). Genetic and morphological divergence in the warm-water planktonic foraminifera genus Globigerinoides. *PLoS One*, *14*(12), 1–30. https://doi.org/10.1371/journal.pone.0225246

Nagai, Y., Uematsu, K., Chen, C., Wani, R., Tyszka, J., & Toyofuku, T. (2018). Weaving of biomineralization framework in rotaliid foraminifera: Implications for paleoceanographic proxies. *Biogeosciences*, *15*(22), 6773–6789. https://doi.org/10.5194/bg-15-6773-2018

Nagai, Y., Uematsu, K., Wani, R., & Toyofuku, T. (2018). Reading the fine print: Ultra-microstructures of foraminiferal calcification revealed using focused ion beam microscopy. *Frontiers in Marine Science*, *5*, 1–15. https://doi.org/10.3389/fmars.2018.00067

Nakajima, K., Nagai, Y., Suzuki, M., Oaki, Y., Naito, K., Tanaka, Y., et al. (2016). Mesoscopic crystallographic textures on shells of a hyaline radial foraminifer: Ammonia Beccarii. *CrystEngComm*, *18*(37), 7135–7139. https://doi.org/10.1039/c6ce01611a

Nehrke, G., Keul, N., Langer, G., deNooijer, L. J., Bijma, J., & Meibom, A. (2013). A new model for biomineralization and trace-element signatures of foraminifera tests. *Biogeosciences Discussions*, *10*(6), 9797–9818. https://doi.org/10.5194/bgd-10-9797-2013

Nielsen, L. C., De Yoreo, J. J., & DePaolo, D. J. (2013). General model for calcite growth kinetics in the presence of impurity ions. *Geochimica et Cosmochimica Acta*, *115*, 100–114. https://doi.org/10.1016/j.gca.2013.04.001

Ní Fhlaithearta, S., Ernst, S. R., Nierop, K. G. J., deLange, G. J., & Reichart, G. J. (2013). Molecular and isotopic composition of foraminiferal organic linings. *Marine Micropaleontology*, *102*, 69–78. https://doi.org/10.1016/j.marmicro.2013.06.004

Öğretmen, N., Schiebel, R., Jochum, K. P., Stoll, B., Weis, U., Repschläger, J., et al. (2020). Deep thermohaline circulation across the closure of the central American Seaway. *Paleoceanography and Paleoclimatology*, *35*(12). https://doi.org/10.1029/2020PA004049

Oaki, Y., Kotachi, A., Miura, T., & Imai, H. (2006). Bridged nanocrystals in biominerals and their biomimetics: Classical yet modern crystal growth on the nanoscale. *Advanced Functional Materials*, *16*(12), 1633–1639. https://doi.org/10.1002/adfm.200600262

Ogino, T., Suzuki, T., & Sawada, K. (1987). The formation and transformation mechanism of calcium carbonate in water. *Geochimica et Cosmochimica Acta*, *51*(10), 2757–2767. https://doi.org/10.1016/0016-7037(87)90155-4

Pabich, S., Vollmer, C., & Gussone, N. (2020). Investigating crystal orientation patterns of foraminiferal tests by electron backscatter diffraction analysis. *European Journal of Mineralogy*, *32*(6), 613–622. https://doi.org/10.5194/ejm-32-613-2020

Paquette, J., & Reeder, R. J. (1990). Single-crystal X-ray structure refinements of two biogenic magnesian calcite crystals. *American Mineralogist*, *75*(9–10), 1151–1158.

Pearson, P. N., Ditchfield, P. W., Singano, J., Harcourt-Brown, K. G., Nicholas, C. J., Olsson, R. K., et al. (2001). Warm tropical sea surface temperatures in the Late Cretaceous and Eocene epochs. *Nature*, *413*(6855), 481–487. https://doi.org/10.1038/35097000

Pokroy, B., Fitch, A., & Zolotoyabko, E. (2006). The microstructure of biogenic calcite: A view by high-resolution synchrotron powder diffraction. *Advanced Materials*, *18*(18), 2363–2368. https://doi.org/10.1002/adma.200600714

Pokroy, B., Quintana, J. P., Caspi, E. N., Berner, A., & Zolotoyabko, E. (2004). Anisotropic lattice distortions in biogenic aragonite. *Nature Materials*, *3*(12), 900–902. https://doi.org/10.1038/nmat1263

Polishchuk, I., Bracha, A. A., Bloch, L., Levy, D., Kozachkevich, S., Etinger-Geller, Y., et al. (2017). Coherently aligned nanoparticles within a biogenic single crystal: A biological prestressing strategy. *Science*, *358*(6368), 1294–1298. https://doi.org/10.1126/science.aaj2156

Pouget, E. M., Bomans, P. H. H., Goos, J. A. C. M., Frederik, P. M., deWith, G., & Sommerdijk, N. A. J. M. (2009). The initial stages of template-controlled CaCO 3 formation revealed by cryo-TEM. *Science*, *323*(5920), 1455–1458. https://doi.org/10.1126/science.1169434

Rae Cho, K., Kim, Y.-Y., Yang, P., Cai, W., Pan, H., Kulak, A. N., et al. (2016). Direct observation of mineral–organic composite formation reveals occlusion mechanism. *Nature Communications*, *7*(1), 10187. https://doi.org/10.1038/ncomms10187

Rao, A., & Cölfen, H. (2017). Mineralization schemes in the living world: Mesocrystals. In A. E. S. van Driessche, M. Kellermeier, L. G. Benning, & D. Gebauer (Eds.), *New perspectives on mineral nucleation and growth: From solution precursors to solid materials* (pp. 155–183). Springer International Publishing. https://doi.org/10.1007/978-3-319-45669-0_8

Rao, A., & Cölfen, H. (2018). From solute, fluidic and particulate precursors to complex organizations of matter. *The Chemical Record*, *18*(7–8), 1203–1221. https://doi.org/10.1002/tcr.201800003

Rao, A., Roncal-Herrero, T., Schmid, E., Drechsler, M., Scheffner, M., Gebauer, D., et al. (2019). On biomineralization: Enzymes switch on mesocrystal assembly. *ACS Central Science*, *5*(2), 357–364. https://doi.org/10.1021/acscentsci.8b00853

Raz, S., Hamilton, P. C., Wilt, F. H., Weiner, S., & Addadi, L. (2003). The transient phase of amorphous calcium carbonate in sea urchin larval spicules: The involvement of proteins and magnesium ions in its formation and stabilization. *Advanced Functional Materials*, *13*(6), 480–486. https://doi.org/10.1002/adfm.200304285

Read, E. (2019). *Diffraction and spectroscopy of marine calcite biominerals: Insights into structure and geochemistry*. Retrieved from https://www.repository.cam.ac.uk/handle/1810/307395

Repschläger, J., Auderset, A., Blanz, T., Bremer, K., Böttner, C., Eich, C., et al. (2018). *North Atlantic Subtropical Gyre Azores front (NASGAF). September 10, 2016-October 7, 2016*. Cruise No. MSM58/1.

Robbins, L. L., & Brew, K. (1990). Proteins from the organic matrix of core-top and fossil planktonic foraminifera. *Geochimica et Cosmochimica Acta*, *54*(8), 2285–2292. https://doi.org/10.1016/0016-7037(90)90052-M

Robbins, L. L., & Donachy, J. E. (1991). *Mineral Regulating Proteins from Fossil Planktonic Foraminifera* (pp. 139–148). https://doi.org/10.1021/bk-1991-0444.ch010

Rodriguez-Blanco, J. D., Shaw, S., & Benning, L. G. (2011). The kinetics and mechanisms of amorphous calcium carbonate (ACC) crystallization to calcite, via vaterite. *Nanoscale*, *3*(1), 265–271. https://doi.org/10.1039/c0nr00589d

Rodriguez-Navarro, C., Burgos Cara, A., Elert, K., Putnis, C. V., & Ruiz-Agudo, E. (2016). Direct nanoscale imaging reveals the growth of calcite crystals via amorphous nanoparticles. *Crystal Growth & Design*, *16*(4), 1850–1860. https://doi.org/10.1021/acs.cgd.5b01180

Rodríguez-Navarro, C., Ruiz-Agudo, E., Harris, J., & Wolf, S. E. (2016). Nonclassical crystallization in vivo et in vitro (II): Nanogranular features in biomimetic minerals disclose a general colloid-mediated crystal growth mechanism. *Journal of Structural Biology*, *196*(2), 260–287. https://doi.org/10.1016/j.jsb.2016.09.005

Sabbatini, A., Bédouet, L., Marie, A., Bartolini, A., Landemarre, L., Weber, M. X., et al. (2014). Biomineralization of Schlumbergerella floresiana, a significant carbonate-producing benthic foraminifer. *Geobiology*, *12*(4), 289–307. https://doi.org/10.1111/gbi.12085

Schiebel, R. (2002). Planktic foraminiferal sedimentation and the marine calcite budget. *Global Biogeochemical Cycles*, *16*(4), 3–21. https://doi.org/10.1029/2001GB001459

Schiebel, R., & Hemleben, C. (2017). *Planktic foraminifers in the modern ocean: Ecology, biogeochemistry, and application*. Springer Berlin Heidelberg. https://doi.org/10.1007/978-3-662-50297.6

Schmidt, N.-H., & Olesen, N. (1989). Computer-aided determination of crystal-lattice orientation from electron-channeling patterns in the SEM. *The Canadian Mineralogist*, *27*, 15–22.

Seknazi, E., & Pokroy, B. (2018). Residual strain and stress in Biocrystals. *Advanced Materials*, *30*(41), 1707263. https://doi.org/10.1002/adma.201707263

Seto, J., Ma, Y., Davis, S. A., Meldrum, F. C., Gourrier, A., Kim, Y.-Y., et al. (2012). Structure-property relationships of a biological mesocrystal in the adult sea urchin spine. *Proceedings of the National Academy of Sciences*, *109*(10), 3699–3704. https://doi.org/10.1073/pnas.1109243109

Sexton, P. F., Wilson, P. A., & Pearson, P. N. (2006). Microstructural and geochemical perspectives on planktic foraminiferal preservation: "Glassy" versus "frosty". *Geochemistry, Geophysics, Geosystems*, *7*(12). https://doi.org/10.1029/2006GC001291

Sommerdijk, N. A. J. M., & deWith, G. (2008). Biomimetic $CaCO_3$ mineralization using designer molecules and interfaces. *Chemical Reviews*, *108*(11), 4499–4550. https://doi.org/10.1021/cr078259o

Spanos, N., & Koutsoukos, P. G. (1998). The transformation of vaterite to calcite: Effect of the conditions of the solutions in contact with the mineral phase. *Journal of Crystal Growth*, *191*(4), 783–790. https://doi.org/10.1016/S0022-0248(98)00385-6

Stathoplos, L., & Tuross, N. (1991). Mineral-associated proteins from modern planktonic foraminifera. In S. Suga, & H. Nakahara (Eds.), *Mechanisms and phylogeny of mineralization in biological systems*. Springer Japan. https://doi.org/10.1007/978-4-431-68132-8

STOECie GmbH. (2011). *WinXPOW*.

Sturm, E. V., & Cölfen, H. (2016). Mesocrystals: Structural and morphogenetic aspects. *Chemical Society Reviews*, *45*(21), 5821–5833. https://doi.org/10.1039/c6cs00208k

Towe, K., & Cifelli, R. (1967). Wall ultrastructure in the calcareous foraminifera: Crystallographic aspects and a model for calcification. *Journal of Paleontology*, *41*(3), 742–762.

Toyofuku, T., Matsuo, M. Y., De Nooijer, L. J., Nagai, Y., Kawada, S., Fujita, K., et al. (2017). Proton pumping accompanies calcification in foraminifera. *Nature Communications*, *8*(1), 6–11. https://doi.org/10.1038/ncomms14145

Tyszka, J., Bickmeyer, U., Raitzsch, M., Bijma, J., Kaczmarek, K., Mewes, A., et al. (2019). Form and function of F-actin during biomineralization revealed from live experiments on foraminifera. *Proceedings of the National Academy of Sciences of the United States of America*, *116*(10), 4111–4116. https://doi.org/10.1073/pnas.1810394116

Tyszka, J., Godos, K., Goleń, J., & Radmacher, W. (2021). Foraminiferal organic linings: Functional and phylogenetic challenges. *Earth-Science Reviews*, *220*, 103726. https://doi.org/10.1016/j.earscirev.2021.103726

van Dijk, I., Barras, C., de Nooijer, L. J., Mouret, A., Geerken, E., Oron, S., & Reichart, G.-J. (2019). Coupled calcium and inorganic carbon uptake suggested by magnesium and sulfur incorporation in foraminiferal calcite. *Biogeosciences*, *16*(10), 2115–2130. https://doi.org/10.5194/bg-16-2115-2019

van Dijk, I., Nooijer De, L. J., & Reichart, G. J. (2017). Trends in element incorporation in hyaline and porcelaneous foraminifera as a function of pCO2. *Biogeosciences*, *14*(3), 497–510. https://doi.org/10.5194/bg-14-497-2017

Wang, J., & Becker, U. (2009). Structure and carbonate orientation of vaterite ($CaCO_3$). *American Mineralogist*, *94*(2–3), 380–386. https://doi.org/10.2138/am.2009.2939

Weiner, S., & Erez, J. (1984). Organic matrix of the shell of the foraminifer, Heterostegina depressa. *Journal of Foraminiferal Research*, *14*(3), 206–212. https://doi.org/10.2113/gsjfr.14.3.206

Weiner, S., & Lowenstam, H. (1986). Organization of extracellularly mineralized tissues: A Comparative study of biological crystal growt. *Critical Reviews in Biochemistry*, *20*(4), 365–408. https://doi.org/10.3109/10409238609081998

Wolf, S. E. (2021). Bioinorganic and bioinspired solid-state chemistry: From classical crystallization to nonclassical synthesis concepts. In *Synthetic inorganic chemistry* (pp. 433–490). Elsevier. https://doi.org/10.1016/B978-0-12-818429-5.00006-5

Wolf, S. E., Böhm, C. F., Harris, J., Demmert, B., Jacob, D. E., Mondeshki, M., et al. (2016). Nonclassical crystallization in vivo et in vitro (I): Process-structure-property relationships of nanogranular biominerals. *Journal of Structural Biology*, *196*(2), 244–259. https://doi.org/10.1016/j.jsb.2016.07.016

Wolf, S. E., Lieberwirth, I., Natalio, F., Bardeau, J. F., Delorme, N., Emmerling, F., et al. (2012). Merging models of biomineralisation with concepts of nonclassical crystallisation: Is a liquid amorphous precursor involved in the formation of the prismatic layer of the Mediterranean Fan Mussel Pinna nobilis? *Faraday Discussions*, *159*, 433–448. https://doi.org/10.1039/c2fd20045g

Yin, X., Griesshaber, E., Checa, A., Nindiyasari-Behal, F., Sánchez-Almazo, I., Ziegler, A., & Schmahl, W. W. (2021). Calcite crystal orientation patterns in the bilayers of laminated shells of benthic rotaliid foraminifera. *Journal of Structural Biology*, *213*(2), 107707. https://doi.org/10.1016/j.jsb.2021.107707

Yoshimura, T., Tamenori, Y., Suzuki, A., Kawahata, H., Iwasaki, N., Hasegawa, H., et al. (2017). Altervalent substitution of sodium for calcium in biogenic calcite and aragonite. *Geochimica et Cosmochimica Acta*, *202*, 21–38. https://doi.org/10.1016/j.gca.2016.12.003

Zhu, G., Sushko, M. L., Loring, J. S., Legg, B. A., Song, M., Soltis, J. A., et al. (2021). Self-similar mesocrystals form via interface-driven nucleation and assembly. *Nature*, *590*(7846), 416–422. https://doi.org/10.1038/s41586-021-03300-0

Zolotoyabko, E. (2017). Anisotropic lattice distortions in biogenic minerals originated from strong atomic interactions at organic/inorganic interfaces. *Advanced Materials Interfaces*, *4*(1), 1600189. https://doi.org/10.1002/admi.201600189

Zolotoyabko, E., Caspi, E. N., Fieramosca, J. S., Von Dreele, R. B., Marin, F., Mor, G., et al. (2010). Differences between bond lengths in biogenic and geological calcite. *Crystal Growth & Design*, *10*(3), 1207–1214. https://doi.org/10.1021/cg901195t